Check for updates

DFT-aided experimental investigation on the electrochemical performance of hetero-interface-functionalized CuO nanoparticle-decorated MoS₂ nanoflowers for energy storage applications†

Muhammad Rakibul Islam, [iD] *[a] Nahid Farzana,[b] Md. Rajbanul Akhond,[c] Mizanur Rahaman,[a] Md Jahidul Islam[c] and Ishtiaque M. Syed[b]

The present study employed a simple hydrothermal approach to synthesize CuO nanoparticle-decorated MoS₂ nanoflowers (MoS₂/CuO). The effect of the concentration of CuO(0, 1, 2 wt%, 4, and 6 wt%) on the surface morphological, structural, optical, and electrochemical properties of the composite nanomaterials was studied. Surface imaging reveals the 3D nanoflower morphology of MoS₂ and MoS₂/CuO nanocomposites. The structural analysis showed a change in the structural parameters due to the incorporation of CuO. Due to the incorporation of CuO, it was determined that the optical band gap of nanocomposites dropped from 1.43 eV to 1.08 eV. The electrochemical performance of the composites was found to be significantly improved due to the decoration of CuO, and the composition with 4 wt% CuO showed the best electrochemical performance possessing a specific capacitance of 336 F g⁻¹ together with 90% capacitive retention after 6000 charge/discharge cycles. The electrochemical performance of the nanocomposite is enhanced by several factors, such as a large surface area, improved structural stability, and minimal charge transfer resistance. Density functional theory was used to theoretically understand the influence of CuO nanoparticles on the electronic and optical properties, as well as the electrochemical performance of the nanocomposite. Theoretical calculations showed that CuO prevents the restacking of MoS₂ layers, increasing its active surface area. Hybridization in the interface region between Mo and O orbitals increases states near the Fermi level, leading to higher conductivity, specific capacitance, and a lower optical band gap. The charge transfer from MoS₂ to CuO creates a strong intrinsic electric field that improves electron transfer, resulting in longer charging and discharging times and enhanced electrochemical performance.

1. Introduction

Electrochemical energy storage materials and technologies have drawn significant research attention due to the growing demand for effective, eco-friendly, and renewable energy sources.[1–3] Batteries and electrochemical capacitors are primarily used for energy storage applications. Among them, electrochemical capacitors have gained tremendous interest due to their excellent capacitance, cyclic capacity, and low internal resistance, energy density, and power density.[4] These distinctive features make them suitable candidates for energy storage devices in various fields, such as transportation, renewable energy, and consumer electronics.

Layered structured materials have recently drawn considerable attention as electrode materials because of their unique material characteristics and diverse applications. Among the numerous layered materials, 2D layered MoS₂, made up of an S–Mo–S unit atomic tri-layer, is considered an appropriate candidate for energy storage applications. The tight covalent bonds between Mo and S and the van der Waals force that holds the S–Mo–S layer together in MoS₂ make it easier for charge carriers from the electrolyte to intercalate towards the inner layer without causing significant deformation of the crystalline structure, yielding better capacitive performance.[5,6] Several techniques, including micromechanical exfoliation and CVD, are commonly used to synthesize layer-structured MoS₂.[7] These methods can achieve the most desirable properties when MoS₂ is synthesized. However, the high cost, complex setup, and low production yield of these methods restrict the large-

a Department of Physics, Bangladesh University of Engineering and Technology, Dhaka, Bangladesh. E-mail: rakibul@phy.but.ac.bd

b Department of Physics, University of Dhaka, Dhaka, Bangladesh

c Department of Materials and Metallurgical Engineering, Bangladesh University of Engineering and Technology, Dhaka, Bangladesh

scale manufacturing of MoS_2-based devices. In contrast, the MoS_2 nanoflower synthesized through a facile hydrothermal process may offer a high-yield production of nanomaterials using a simple, easy, and economical route. Also, the large surface area and channels for ion intercalation/de-intercalation provided by the nanoflower structure make it favorable for energy storage applications.

Although MoS_2 shows many promising properties, its low electrical conductivity and specific capacitance result in smaller specific energy and poor cyclic stability, which is unsuitable for electrochemical energy storage applications.[7–9] Combining MoS_2 with metal oxide nanoparticles is a valuable technique to boost its electrochemical performance. Metal oxide nanoparticles provide better conductivity, and their rapid redox kinetics can increase the charge carrier's transportation rate when incorporating the MoS_2 nanostructure, thereby improving the capacitive performance.[10,11] Different metal oxide nanoparticles, including NiO, MnO_2, TiO_2, and Co_3O_4, have been incorporated to improve the electrochemical properties of MoS_2 nanomaterials.[11–14] Wang et al.[15] reported the synthesis of MoS_2/Mn_3O_4 composite nanomaterials by a combined hydrothermal and chemical precipitation method. They found that incorporating Mn_3O_4 improved the capacitance of layer-structured MoS_2 from 47.2 F g^{-1} to 119.3 F g^{-1}. Chanda et al.[16] showed that a specific capacitance of 152.22 F g^{-1} at a current density of 0.1 A g^{-1} is achieved when TiO_2 spheres are added into MoS_2 nanoflakes. Ahmad et al.[14] fabricated Co_3O_4-decorated MoS_2 nanoflowers by a simple hydrothermal route. They found that the incorporation of 4 wt% Co_3O_4 increases the specific capacitance by 135% compared with MoS_2. Additionally, they demonstrated that 87% cyclic stability was maintained after 10 000 charging/discharging cycles.

CuO is a promising candidate for electrochemical applications due to its distinctive capacitive properties and good electronic conductivity. Previous studies showed that when hybridized with MoS_2, the CuO-based heterostructure provides an enlarged specific surface area, changes in surface states, and modifies the energy states, resulting in improved photoluminescence properties and enhanced catalytic performance. The MoS_2/CuO heterojunction has also shown a number of promising applications, such as a non-enzymatic glucose sensor, photocatalyst, humidity sensor, photodetector, etc.[17,18] The enhanced surface area and the increasing structural stability of the MoS_2/CuO nanostructure may provide better electrochemical performance. More recently, Awasthi et al. reported the preparation of p–n heterostructural CuO/MoS_2 composites for supercapacitor applications by mixing MoS_2 nanosheets with urchin-like CuO particles.[19] However, MoS_2 nanosheets exhibit inadequate electrochemical performance because of the small electronic conductivity and significant surface energy of 2D MoS_2 nanosheets. Furthermore, synthesizing MoS_2 nanosheets from their bulk is time-consuming and may result in a low yield of nanosheets. In this respect, the synthesis of MoS_2 nanoflowers through the hydrothermal process may provide an economical, easy, and high-yield path for the industrial fabrication of MoS_2-based devices.

To consider the application, it is necessary to comprehend the impact of CuO nanoparticles on the electronic structure and capacitive performance of MoS_2. Therefore, experimental and theoretical analyses on CuO-decorated MoS_2 are required, which have never been performed. To understand the properties of materials in a way that is both accurate and computationally efficient, density functional theory (DFT) can be utilized. Density functional theory can effectively predict optical, electronic, and electrochemical systems and helps design new materials with improved properties. The charge transfer properties of different materials and how they interact in an electrochemical environment can also be investigated using DFT.[20] Previously, Li et al.[19] calculated the theoretical adsorption energy of the MoS_2/CuO structure using DFT, where H_2O was taken as the adsorbate.

In this study, we prepared CuO-decorated MoS_2 nanoflowers through a simple synthesis approach with varied amounts of CuO nanoparticles (NPs). The effect of the concentration of CuO nanoparticles was studied using different characterization techniques. FESEM images showed how CuO nanoparticles change the morphology of MoS_2 nanoflowers. The incorporation of CuO nanoparticles reduces the optical band gap from 1.43 eV to 1.08 eV. CuO was found to enhance the capacitive properties of MoS_2, with the highest specific capacitance of 336.72 F g^{-1} achieved at a current density of 0.1 A g^{-1}. The composite nanomaterials demonstrate an excellent capacitance retention of 90% even after 6000 cycles. DFT simulation was performed to obtain theoretical insight into the impact of CuO on the electronic, optical, charge transfer, and quantum capacitance of MoS_2. The theoretical study supports our experimental results as it also predicts a decreased optical band gap due to CuO incorporation. Quantum capacitance calculations provide similar values and trends, reporting a C_Q value of around 61.01 F g^{-1} for pure MoS_2 and an average value of 351.70 F g^{-1} for CuO-incorporated MoS_2. Moreover, these calculations shed further light on novel mechanisms through which CuO plays a synergistic role in improving the electrochemical performance of pristine MoS_2.

2. Materials and methods

2.1. Materials

Analytical-grade chemicals were used in this experiment. Sodium molybdate dihydrate ($Na_2MoO_4 \cdot 2H_2O$), dimethyl sulfoxide (C_2H_6OS), copper nitrate ($Cu(NO_3)_2 \cdot 3H_2O$) and citric acid were received from Mark India. Thiourea (CH_4N_2S), polyvinyl alcohol (C_2H_4O), and sodium sulfate (Na_2SO_4) were purchased from Research Lab, India.

2.2. Synthesis of MoS_2 and MoS_2/CuO nanocomposites

To prepare MoS_2 nanoflowers through a facile hydrothermal approach, sodium molybdate dihydrate and thiourea as the respective sources for Mo and S were utilized.[14] A predetermined quantity of the precursors was dissolved in DI water and agitated vigorously. Subsequently, the solution was placed in a Teflon-lined autoclave at 200 °C for 24 hours. Following

centrifugation, the precipitate underwent a washing procedure involving DI water and ethanol. The MoS_2 nanoflower was obtained by drying the resulting black powder at a temperature of 80 °C for several hours.

CuO was prepared by the solution combustion method.[21] The FESEM images show the particle-like morphology of CuO, which is presented in Fig. SF1(a) (ESI†). The typical particle size of CuO varies between 30–40 nm. Fig. SF1(b) (ESI†) presents the XRD pattern of CuO nanoparticles. Diffraction peaks at 32.52°, 35.57°, 38.73°, 48.83°, 53.58°, 58.22°, 61.54°, 66.26°, and 68.13° correspond to the crystallographic planes (110), (11−1), (111), (20−2), (020), (202), (11−3), (21−1) and (220), respectively (JCPDS card no. 05-0661). The as-prepared CuO exhibits a monoclinic crystal structure without indicating a secondary phase. The narrow width of the sharp peaks denotes the crystalline nature of the NPs.

To prepare MoS_2/CuO nanocomposites, CuO nanoparticles (1, 2, 4, and 6 wt% CuO) were added to 50 mL of DI water and sonicated for 2 hours using a bath sonicator. Sodium molybdate dihydrate, and thiourea were added in 70 mL of DI water, followed by vigorous stirring. The CuO solution was added to it and stirred for several hours. The solution was kept in an autoclave at 200 °C for 24 hours. The resulting precipitate was then centrifuged, followed by washing with DI water and ethanol. The resulting black powder was dried at 80 °C for several hours to produce MoS_2/CuO composites.

2.3. Characterization

The surface of the nanocomposite was examined using a field emission scanning electron microscope (FESEM) (JEOL JSM-7600F). The structural parameters of all samples were analyzed through the X-ray diffraction (XRD) technique. The XRD data were collected utilizing CuK$_\alpha$ radiation (1.5406 Å) with an X-ray diffractometer (RIGAKU Ultima IV). The electrochemical characteristics were studied using a three-electrode setup. The electrolyte solution employed was an aqueous solution of Na_2SO_4 with an ionic concentration of 0.5 M. The experimental setup consisted of a modified graphite working electrode, a platinum foil plate measuring 1 cm × 1 cm, and a silver/silver chloride (Ag/AgCl) counter electrode. An electrochemical working station, model CS-310 (corrtest, China), was utilized to oversee the cyclic voltammetry (CV), galvanostatic charge/discharge (GCD), and electrochemical impedance spectroscopy (EIS). For electrochemical characterization studies, the active material of MoS_2 and MoS_2/CuO composite was mixed with polyvinyl alcohol (C_2H_4O) (4 wt% of the active material) and solvent dimethyl sulfoxide (C_2H_6OS) to produce the working electrode. These mixtures were sonicated for half an hour before depositing 0.4 mg on the graphite electrode.

2.4. Computational methodology

The initial application of DFT calculations was executed using the Vienna *ab initio* simulation package (VASP) software.[22] The present study employed the projector augmented wave (PAW) technique,[23,24] which accounts for the interaction between valence electrons and core ions. This method was originally proposed by Peter Blöchl[24] and implemented in the code developed by G. Kresse.[25] The valence electron configurations of the following elements were taken into consideration: molybdenum (Mo) with a configuration of $4s^2\ 4p^6\ 4d^4\ 5s^2$, sulfur (S) with a configuration of $3s^2\ 3p^6$, copper (Cu) with a configuration of $3d^{10}\ 4s^1$, and oxygen (O) with a configuration of $2s^2\ 2p^4$. Due to the band gap underestimation limitation of the DFT approximation for highly correlated materials, the Hubbard DFT+U correction scheme was used for CuO in this analysis, as originally introduced in ref. 26. The aforementioned methodology is commonly employed in investigating various transition-metal complexes.[27,28] Alternative computation methods, such as the hybrid functional (HSE06)[29] and GW functional,[30] offer greater accuracy, albeit at a significantly higher computational cost. Moreover, dispersion-corrected DFT calculations were employed to capture the van der Waals interaction from the layered structure, which plays a vital role in determining the bandgap as well as quantum capacitance values accurately.[31]

The approximated functional utilized in this study was the Perdew–Burke–Ernzerhof (PBE) functional, which is a form of the generalized gradient approximation (GGA).[32] In all calculations, a plane wave basis set with a cutoff energy of 520 eV was employed. The Monkhorst–Park scheme was utilized to apply an automatically generated K-point grid centered on gamma. The k-point sampling was performed utilizing a spacing of 0.03 units between the two closest points. Ionic relaxation was conducted during geometry optimization until the energy variations and forces acting on individual atoms were less than 10^{-07} eV and 0.03 eV Å^{-1}, respectively. A Hubbard potential of U_{eff} = 7.14 eV was added to the strongly localized 3d orbitals of Cu, based on the value found in the literature.[33] DFT-D3 (semi-empirical-based) type van der Waals corrections were used in the study to account for the dispersion error.

3. Results and discussion

3.1. Surface morphology

Fig. 1(a) and (b) present a 3D flower-like morphology of MoS_2. The thickness of the petals of the flower ranges, on average, between 4 to 7 nm, and they are connected to a common center. Fig. 1(c)–(f) depict the morphology of MoS_2/CuO at various CuO nanoparticle concentrations. Incorporating CuO nanoparticles at low concentrations has little effect on the growth of the nanoflower. Due to ultrasonication and hydrothermal reactions, the CuO nanoparticles were well dispersed in the nanocomposite. In addition, some CuO is observed on the nanopetals of MoS_2 nanoflowers. The thickness of the nanopetals was found to decrease with the incorporation of CuO nanoparticles, which indicates that interaction occurred between MoS_2 and CuO nanoparticles. The reduction in thickness of the nanopetals can accelerate the charge transfer of the MoS_2/CuO nanocomposite.[34] For higher concentrations (6%) of CuO nanoparticles (Fig. 1(f)), the nanopetals were fractured, and the size and morphology of the MoS_2 nanoflower changed. Furthermore, the CuO nanoparticles were found to be agglomerated on the MoS_2 nanoflower. These agglomerations reduce the surface area, active sites, and
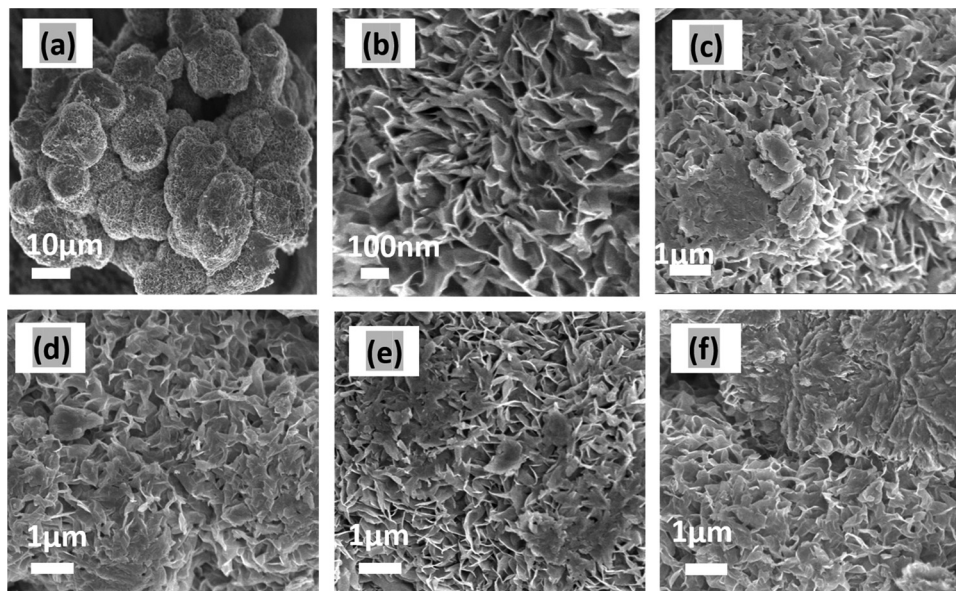
Fig. 1 FESEM images of (a) MoS₂ under low and (b) MoS₂ at high magnification, (c) MoS₂/CuO(1 wt%), (d) MoS₂/CuO(2 wt%), (e) MoS₂/CuO(4 wt%), and (f) MoS₂/CuO(6 wt%).

interfacial interaction, which might diminish the electrochemical performance of the nanocomposite. EDX analysis was performed to study the presence of CuO on MoS₂, and the Fig. SF2 (ESI†) represents the corresponding EDX spectrum. The nanocomposites' elemental contribution is shown in the Table ST1 (ESI†). This confirms the presence of Mo, S, Cu, and O in the MoS₂/CuO nanocomposite.

3.2. Structural properties

Fig. 2 illustrates the XRD patterns for MoS₂ and MoS₂/CuO with different concentrations of CuO. The diffraction peaks for MoS₂ were found at 13.96°, 33.96°, 39.47°, and 59.17° corresponding to the reflections from lattice planes (200), (100), (103) and (110), respectively, and they are in good accordance with JCPDS card number 37-1492, confirming the hexagonal structure of

Fig. 2 XRD pattern of pristine MoS₂ and as prepared MoS₂/CuO composites.

2H-MoS₂.[35–37] The sharp peaks indicate a good crystalline and well-stacked structure of MoS₂.[38] For low concentrations of CuO nanoparticles, the diffraction pattern of MoS₂/CuO composites was found to be similar to that of MoS₂. This suggests that the incorporation of CuO does not change the hexagonal 2H-MoS₂ structure. For higher concentrations (6%) of CuO, two additional peaks were observed at 31.9° and 36.8° corresponding to the (110) and (111) planes for CuO, respectively. This further confirms the presence of CuO in the MoS₂ nanoflower. Fig. 3 depicts the change in different XRD parameters with the amount of CuO in MoS₂. The values of various structural parameters of the synthesized MoS₂ and MoS₂/CuO are presented in Table 1. The incorporation of CuO caused the (002) peak to shift toward a higher 2θ value compared to that of pure MoS₂, suggesting a change in the d-spacing of the composites. The interlayer spacing was calculated using the following equation:

$$2d \sin \theta = n\lambda$$

where d is the interlayer spacing, λ is the X-ray wavelength, and θ is the diffraction angle. The d-spacing of pure MoS₂ was found to be 0.6327 nm, indicating that the 2H-MoS₂ nanoflower was growing well along the c-axis. The d-spacing of MoS₂/CuO composites was found to be smaller than that of pristine MoS₂ and reduced with the concentration of CuO. This change in d-spacing might have been because of an enhanced crystallite size to accommodate CuO; the structure may bend slightly, resulting in a shift in the location of the lattice planes.[39]

With the increasing amount of CuO, diffraction peaks became narrower, suggesting a reduction in crystallite size. The crystallite size (L) was determined from the (002) plane using the Scherrer formula[40]
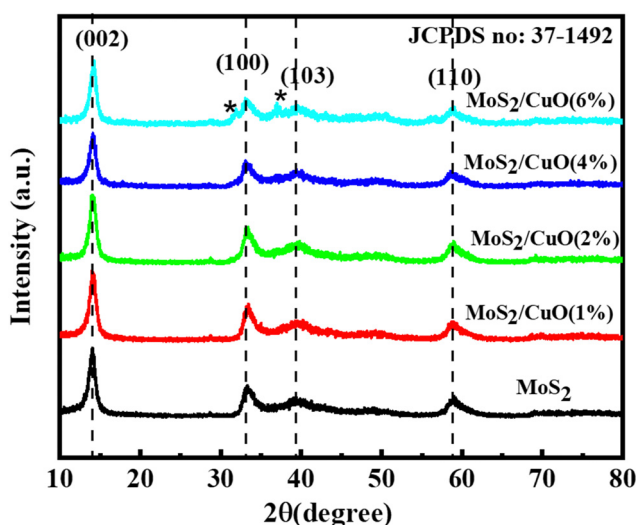
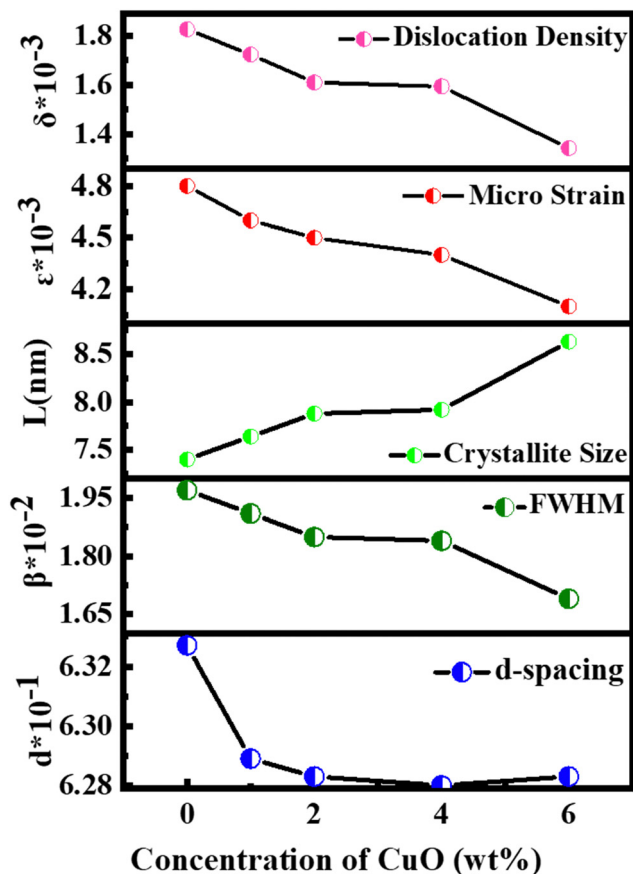$$L = \frac{0.94\lambda}{\beta \cos \theta}$$

Fig. 3 Variation of different XRD parameters as a function of CuO concentration.

Here, λ denotes the X-ray wavelength, θ stands for the diffraction angle, and β is the FWHM of the corresponding diffraction peak. The crystallite size of pure MoS_2 increased from 7.40 nm to 8.93 nm due to the incorporation of CuO. This might be due to the difference in ionic radius between the Cu^{2+} ion (0.072 nm) and Mo^{4+} ion (0.068 nm). Larger crystallites tend to have a more ordered structure, which can lead to better ionic movement and improved electrical conductivity for the nanostructure.

Dislocation density (δ) and microstrain (ε) of the as-prepared samples were measured using the following relationships[41]

$$\delta = \frac{1}{L^2}$$

$$\varepsilon = \frac{\beta}{4\tan\theta}$$

where L, θ, and β denote the crystallite size, diffraction angle, and FWHM of the diffraction peak, respectively.

With the increase in concentration of CuO from 0% to 6%, the value of δ of the nanocomposites was found to be reduced from 18.26×10^{-3} to 13.43×10^{-3}. The microstrain in MoS_2 was also found to be reduced from 4.8×10^{-3} to 4.1×10^{-3} due to the incorporation of CuO nanoparticles. When CuO was incorporated into the MoS_2 structure, atoms bound in non-equilibrium positions might have shifted to more equilibrium places, resulting in a reduction in strain.[42] And this ordered arrangement of particles in the crystal lattice allows for easier movement of electrons, which is necessary for electrical conductivity.

3.3. Optical properties

The optical characteristics of all samples have been investigated *via* analysis of the diffuse reflectance spectra. The absorbance (A) and diffuse reflectance (R) of material are correlated by the Kubelka–Munk (K–M) function, ($F(R)$), as follows:

$$F(R) = \frac{(1-R)^2}{2R} = \frac{k}{s} = \frac{2.303 \times A}{s \times d}$$

where absorption and scattering coefficients are represented by k and S, while A and d represent the absorbance and thickness, respectively, of the sample. Fig. 4 shows the K–M function for MoS_2 and MoS_2/CuO nanocomposites. It was found that with the incorporation of CuO into the MoS_2 nanoflowers, the absorbance increased significantly, suggesting a decrease in the optical bandgap in MoS_2/CuO composites. Fig. 5 presents the optical band gap of all the samples, which is calculated by plotting corresponding $(F(R)h\nu)^{1/2}$ *vs.* photon energy ($h\nu$). The estimated band gap of MoS_2/CuO composites for different concentrations of CuO nanoparticles is tabulated in Table 2. The optical band gap of MoS_2 reduced after the decoration of CuO nanoparticles. The optical bandgap of MoS_2 nanoflowers declined from 1.43 eV to 1.08 eV with the increase in CuO concentrations, which align with the previously reported results.[43] The incorporation of CuO might introduce additional states near the forbidden energy gap, which can reduce the energy required to excite an electron from the valence band to the conduction band.[44]

3.4. Electrochemical properties

Cyclic voltammetry was conducted within a potential window between -0.3 V and 0.2 V at different scan rates (5 mV s^{-1} to 100 mV s^{-1}). The obtained quasi-rectangular CV curves (Fig. 6(a)–(e)) indicate that the pseudocapacitive mechanism dominates the charge transfer process.[45] The area under the CV curve increases with the scanning rate and the current because

Table 1 Structural parameters of MoS_2 and MoS_2/CuO nanocomposites

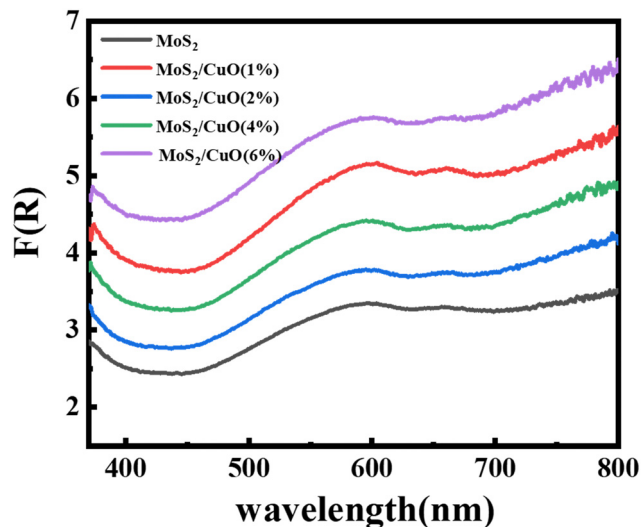| Samples	d-Spacing (nm)	FWHM $\times 10^{-2}$ β (radian)	Crystallite size L (nm)	Dislocation density $\delta \times 10^{-3}$	Micro strain $\varepsilon \times 10^{-3}$
MoS_2	0.6327	1.97	7.40	18.26	4.8
MoS_2/CuO(1%)	0.6289	1.91	7.64	17.23	4.6
MoS_2/CuO(2%)	0.6283	1.85	7.88	16.10	4.5
MoS_2/CuO(4%)	0.6280	1.84	7.92	15.94	4.4
MoS_2/CuO(6%)	0.6283	1.69	8.63	13.43	4.1

Paper

Materials Advances

Fig. 4 Kubelka–Munk plot, $F(R)$ of MoS$_2$ and its composite with different concentrations of CuO derived from diffuse reflectance spectra.

Table 2 The optical band gap of MoS$_2$ and MoS$_2$/CuO nanocomposites

Sample	Optical bandgap (eV)
MoS$_2$	1.43
MoS$_2$/CuO(1%)	1.40
MoS$_2$/CuO(2%)	1.37
MoS$_2$/CuO(4%)	1.28
MoS$_2$/CuO(6%)	1.08

nanoparticles is shown in the Fig. SF3 (ESI†). The deviation from the symmetric and triangular form is caused by the reversible conversion reaction occurring during the measurement procedure, indicating the pseudocapacitive charge storage mechanism.[47] Fig. 7(f) illustrates a GCD plot of MoS$_2$ and MoS$_2$/CuO nanocomposites for different concentrations of CuO at a constant current density. The specific capacitance (C_s) can be measured using the following relationship,

$$C_s = \frac{I\Delta t}{m\Delta V}$$

where I is the applied current, Δt is the discharging time, m is the deposited mass, and ΔV is the potential window. Table 3 shows that the value of C_s for MoS$_2$ is 58.07 F g^{-1} and increases with the amount of CuO. The highest capacitance, 336.23 F g^{-1}, at a current density of 0.1 A g^{-1}, was achieved for MoS$_2$/CuO(4 wt%). However, a further increase in CuO concentration to 6 wt% reduced specific capacitances to 189.14 F g^{-1}. The specific capacitances were also reduced as the current density increased due to inadequate redox reactions at the electrolyte/electrode interface.[48] The specific capacitance for CuO was estimated to be 78.2 F g^{-1} at a current density of 0.1 A g^{-1} (Fig. SF3, ESI†).

The energy density (E) and power density (P) of MoS$_2$ and MoS$_2$/CuO composites were estimated using the following equations:

of the partial intercalation/de-intercalation of electrolyte ions in the electrode. The curves deviated from the ideal rectangular shape, possibly due to the electrolyte ions' temporary movement at the electrode surface.[46] The CV curves of different samples at 30 mV s^{-1} are presented in Fig. 6(f). The incorporation of CuO nanoparticles leads to an increase in the CV area. The electrochemical reaction of MoS$_2$ and CuO in Na$_2$SO$_4$ solution.

$$MoS_2 + Na^+ + e^- \leftrightarrow MoS - SNa$$

$$CuO + \tfrac{1}{2}H_2O + e^- \leftrightarrow \tfrac{1}{2}Cu_2O + OH^-$$
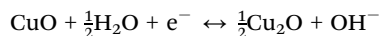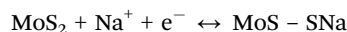
Fig. 7(a)–(e) show the GCD curves of MoS$_2$ and MoS$_2$/CuO at different current densities. In addition, the GCD curve of CuO
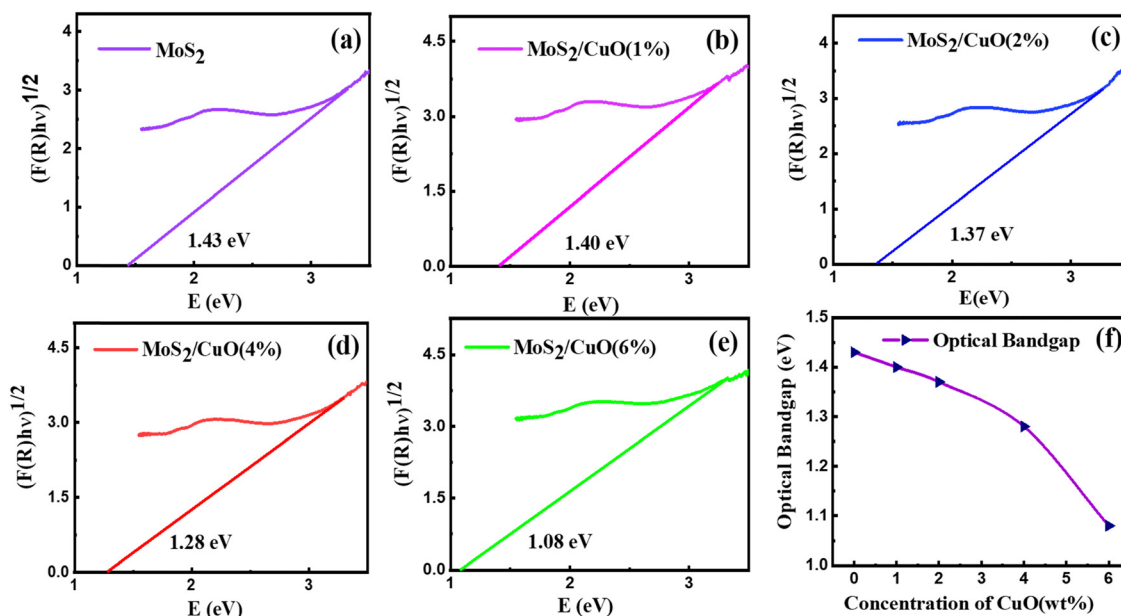

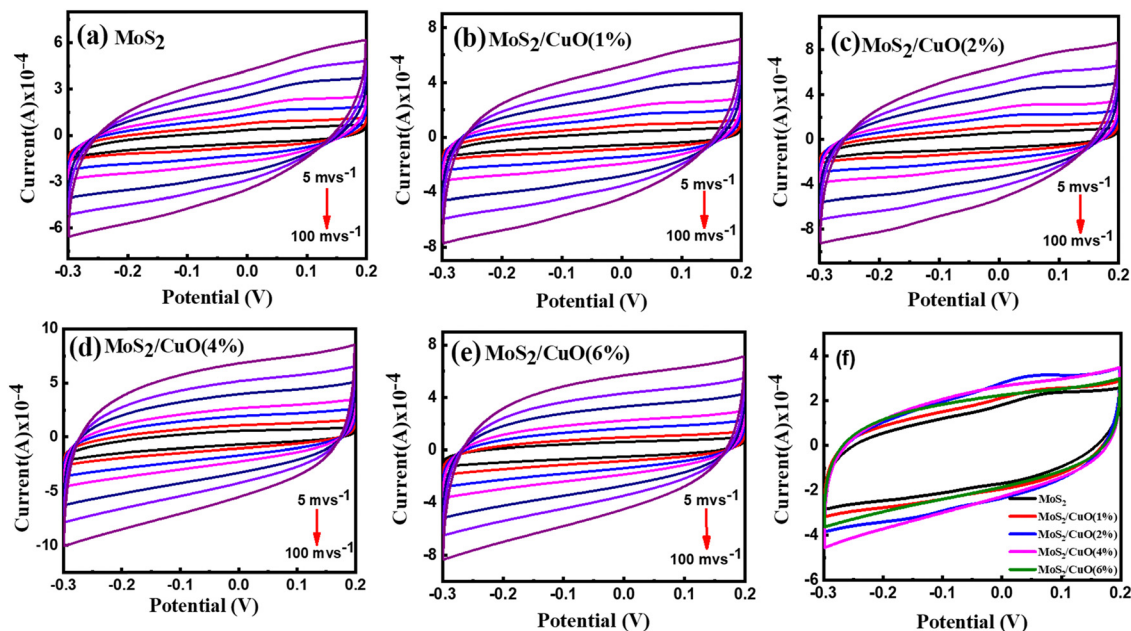Fig. 5 (a)–(e) The Tauc plot of all the as-prepared samples and (f) the variation of the optical bandgap.

Fig. 6 Cyclic voltammetry measurements pristine MoS_2 and as prepared composites at different scan rates (a)–(e) and at 30 mV s^{-1} (f).
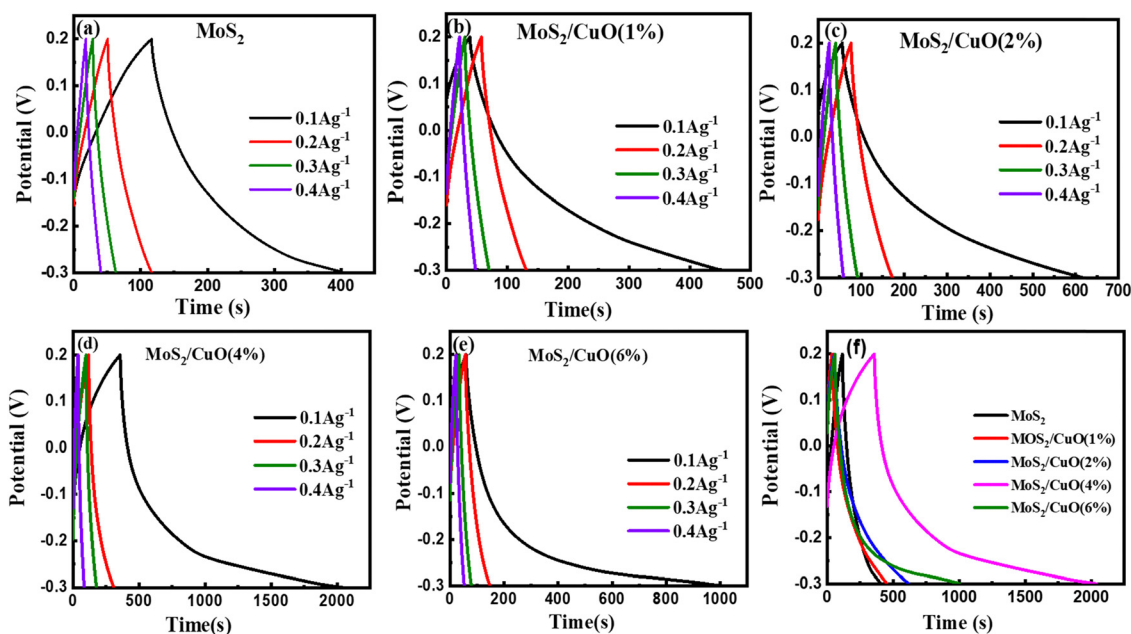

Fig. 7 (a)–(e) Galvanostatic charging discharging (GCD) curves of pristine MoS_2 and as prepared MoS_2/CuO nanocomposites at different current densities and (f) 0.1 A g^{-1} current density of all samples.

$$E = \frac{1}{2} C \Delta V^2$$

$$P = \frac{E}{\Delta t}$$

The estimated values of E and P for all the samples are presented in Table 3, and the MoS_2/CuO(4 wt%) sample gives the highest values.

EIS was implemented to analyze the electrode material's charge-storage mechanism. The Nyquist plot at frequencies between 0.1 HZ to 100 kHz is presented in Fig. 8. This graph displays an inclined line in the lower-frequency region and a semicircular arc in the high-frequency region. A Randles circuit is used to describe the system's faradaic process shown in the inset of Fig. 8, which was constructed to represent the frequency-based electrical performance of the system. The small

Table 3 Specific capacitance, energy density and power density of the prepared samples

Sample	Specific capacitance ($F\ g^{-1}$)	Energy density $W\ h\ kg^{-1}$	Power density $W\ kg^{-1}$
MoS_2	58.07	2.02	24.94
$MoS_2/CuO(1\%)$	82.93	2.88	24.96
$MoS_2/CuO(2\%)$	112.44	3.90	24.97
$MoS_2/CuO(4\%)$	336.23	11.67	24.99
$MoS_2/CuO(6\%)$	189.14	6.57	24.98

Table 4 EIS fitting parameters of MoS_2 and MoS_2/CuO composites

Sample	R_s (Ohm)	R_{el} (Ohm)	R_{ct} (Ohm)
MoS_2	7.40	0.76	26.64
$MoS_2/CuO(1\ wt\%)$	7.78	1.43	56.90
$MoS_2/CuO(2\ wt\%)$	7.57	1.01	51.63
$MoS_2/CuO(4\ wt\%)$	6.28	1.21	10.60
$MoS_2/CuO(6\ wt\%)$	8.47	1.23	20.93

interception of the semicircle to the *x*-axis in the high-frequency region, defined by R_s in the circuit, refers to the bulk resistance of the electrolyte. The semicircle represents the response of charge transfer resistance R_{ct} and the impedance of the electrolyte-electrode surface reaction occurring because of the faradaicreaction R_{el} and EDLC behavior. The Warburg resistance W_o in the circuit symbolizes the impedance caused by the diffusion process and appears in the low-frequency region. The constant phase elements (CPE) in the circuit are capacitive elements. Table 4 presents the EIS fitting parameters of MoS_2 and MoS_2/CuO composites obtained from simulation. The series resistance was found to be similar for all the samples. An observable change in the charge transfer resistance was found. The value of R_{ct} was significantly reduced as the amount of CuO rose, suggesting that the addition of CuO boosted conductivity. The lowest value of R_{ct} was obtained for the $MoS_2/CuO(4\ wt\%)$ composite, suggesting that $MoS_2/CuO(4\ wt\%)$ possesses the best ion conducting ability among all samples. This result is also consistent with CV and GCD results.[49]

The cyclic stability of $MoS_2/CuO(4\ wt\%)$ was investigated for 6000 charging/discharging cycles at a constant current density, shown in Fig. 9(a). A capacitance retention of ~84% was achieved after completing 6000 cycles of operation. A Coulombic efficiency of 113% was achieved in the first cycle, which was found to be 108% in the last cycle. The close interaction of the CuO nanoparticles with MoS_2 improves the cyclic stability of the heterostructure. Fig. 9(b) presents the Nyquist plot of $MoS_2/CuO(4\ wt\%)$ taken before the 1st cycle and after the 6000th cycle of the charging–discharging test. The size of the semicircle in the high-frequency region became larger after 6000 cycles of charging and discharging than that after the 1st cycle. The series resistance dropped after the cycles, whereas the charge transfer resistance R_{ct} and R_{el} increased, revealing a lessening in the conductivity of $MoS_2/CuO(4\ wt\%)$. Because of the repetitive expansion and contraction during charging and discharging, the crystal structure of the active material might have altered or got damaged, causing a decrease in conductivity.[50,51] Table 5 presents the fitting parameters before and after the charge–discharge cycles.

3.5. $MoS_2/CuO(4\ wt\%)$ electrode material

The incorporation of CuO nanoparticles improved the electrochemical performance, and a C_s of 336.23 $F\ g^{-1}$ along with an energy density of 11.67 $W\ h\ kg^{-1}$ has been achieved for the $MoS_2/CuO(4\ wt\%)$ nanocomposite. The layered structure of MoS_2/CuO composites contains abundant channels for electrolyte transportation. The increased concentration of CuO provided a larger surface area for the electrochemical reaction. A large crystallite size caused more intercalation of ions, increasing electronic conductivity up to the amount of 4 wt% of CuO in MoS_2, but a further increase in CuO concentration (*e.g.*, 6 wt%) diminished the electrochemical properties, attributed to the smaller surface area caused by the increase in *d*-spacing.

The material exhibited remarkable cyclic stability and demonstrated outstanding retention of capacitance. The study's notable findings illustrate the potential of the MoS_2/CuO nanocomposite as a viable electrode material for energy storage purposes. Table 6 displays the specific capacitance values of nanocomposite materials based on MoS_2 with varying morphologies. Table 6 displays that the $MoS_2/CuO(4\ wt\%)$ nanocomposite shows a higher specific capacitance than previously reported values. The remarkable outcome was attained due to the nanocomposite's improved interlayer spacing, active sites, and defect states.

3.6. Computational models

According to the experimental findings, semiconducting 2H-MoS_2 has been observed and the {002} planes are the favored orientation of hexagonal 2H-MoS_2 nanoflowers.[58,59] The computational study is performed with the creation of MoS_2 nanoflowers (nF-MoS_2) by utilizing of a 2×2 supercell that consists of bilayer MoS_2 oriented along the [002] direction, as illustrated in Fig. 10c. The interatomic distance between Mo and S atoms is
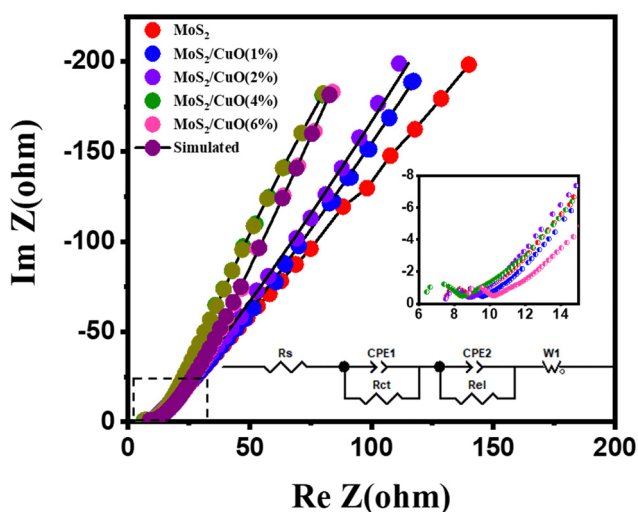
Fig. 8 Modeled and observed Nyquist plots of different samples. The line shows the fitted Nyquist plot for different samples. The inset in the figure shows the magnified image at high frequency and the equivalent circuit used for the simulation.
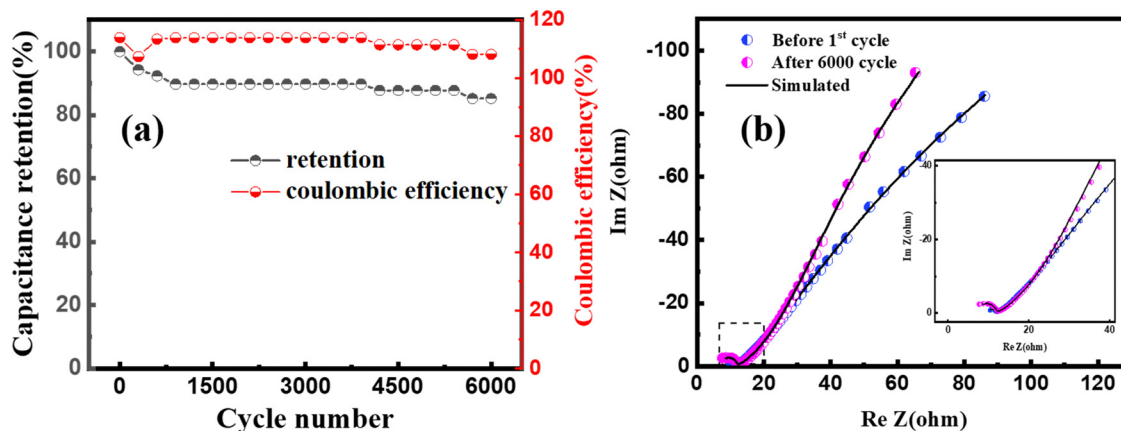
Fig. 9 (a) Cyclic stability performance of MoS$_2$/CuO(4 wt%) at a current density of 5 A g^{-1} (b) Nyquist plot for the MoS$_2$/CuO(4 wt%) sample before the 1st cycle and after 6000 cycles.

Table 5 EIS fitting parameters before and after 6000 cycles of MoS$_2$/CuO(4%) composites

Cycle	R_s (Ohm)	R_{el} (Ohm)	R_{ct} (Ohm)
1	9.93	1.1	10.1
6000	6.80	4.5	20.8

measured to be 2.411 Å. Upon relaxation of the vacuum slab consisting of two layers of MoS$_2$, a slight increase in this bond length is observed. The interlayer spacing was 7.4395 Å and 6.181 Å for the bulk and vacuum surface slab, respectively. The relaxed lattice parameter values of hexagonal MoS$_2$ are reported as $a = b = 6.3806$ Å and $c = 14.879$ Å for the bulk configuration (as shown in Fig. 10a), and $a = b = 6.3687$ Å and $c = 30.3082$ Å for the vacuum slab configuration with a vacuum of 20 Å (as shown in Fig. 10e).

CuO exhibits different oxidation states, crystal structures, and electronic behavior. These differences in the crystal structure and electronic behavior are due to strong electron correlation in CuO.[60] The morphology of CuO nanoparticles depends on the precursor materials and synthesis pathways employed, resulting in a diverse array of geometric configurations. Different surface orientations are observed for various shapes. CuO nanoparticles have a monoclinic crystal structure, and the {111} planes are the most stable surface planes.[61] However, when a heterogeneous nanostructure is formed between nF-MoS$_2$ and nP-CuO, CuO slices are inserted into

Table 6 Comparison of specific capacitance of some reported MoS$_2$-based supercapacitors in the literature

Composite	Morphology	Specific capacitance (F g^{-1})	Ref.
MoS$_2$/C	Nanoflower	201.4 F g^{-1} (0.2 A g^{-1})	52
MoS$_2$/graphene-foam	Nanosheet	48.85 F g^{-1} (1 A g^{-1})	53
MoS$_2$/Ti-plate	Nanosheet	133 F g^{-1} (1 A g^{-1})	54
Ni$_3$S$_4$/MoS$_2$	Nanosheet	108 F g^{-1} (0.5 A g^{-1})	55
SnS$_2$/MoS$_2$	Nanoflower	105.7 F g^{-1} (2.35 A g^{-1})	56
MoS$_2$/ZnO	Nanoflower	42 F g^{-1} (1 A g^{-1})	57
MoS$_2$/CuO	Nanoflower	336.23 F g^{-1} (0.1 A g^{-1})	This work

MoS$_2$ petals, and these CuO slices have a layered structure with {001} planes.[62,63] And on these planes, surface termination is possible for both Cu and O.[64] An appropriate CuO supercell was constructed to model this specific termination behavior. Upon conducting geometric optimization of the CuO bulk supercell, the relaxed structure depicted in Fig. 10(b) exhibits lattice parameters of $a = b \approx 5.9$ Å and $c = 5.17$ Å.

In our study of the nanocomposite interface, we utilized a single layer of the relaxed CuO structure featuring termination by both copper (Cu) and oxygen (O). In both heterostructures, the lattice parameters exhibited identical values for both the a and b directions while maintaining a 20 Å vacuum in the c direction to prevent any potential self-interaction errors. The numerical values of the lattice parameters a and b are determined to be 6.1338 Å, while the parameter c is measured to be 37.3742 Å. The angle between a and b is found to be 105.038°, as depicted in Fig. 10f and g. Additionally, the lattice mismatch parameter α is estimated to be approximately 0.35%, which is computed using the following equation:

$$\alpha = \left(1 - \frac{2A_{MoS_2-CuO(Cu:O)}}{A_{MoS_2} + A_{CuO(Cu:O)}} \right) \times 100\%$$

where A_{MoS_2} and A_{CuO} represent the surface area of pure matter, and A_{MoS_2-CuO} is the overlapping area of composites. The relaxed structures for both Cu and O termination of CuO are presented in Fig. 10(f) and (g), designated as NC$_{Cu}$ and NC$_O$, respectively. Multiple potential global lowest energy configurations can be obtained by utilizing lattice vector matching or alternative modern techniques such as the nonperiodic screening approach.[63,64] Under the presumption that our local minimum configuration supported by experimental observations closely resembles the global minimum configuration for chemisorption of CuO onto the MoS$_2$ slab, the findings presented in the subsequent sections of this paper will remain valid and encompassing.

3.7. Electronic properties

Fig. 11 shows the atomic band projected band structure of MoS$_2$ with an indirect bandgap (a) with and (b) without
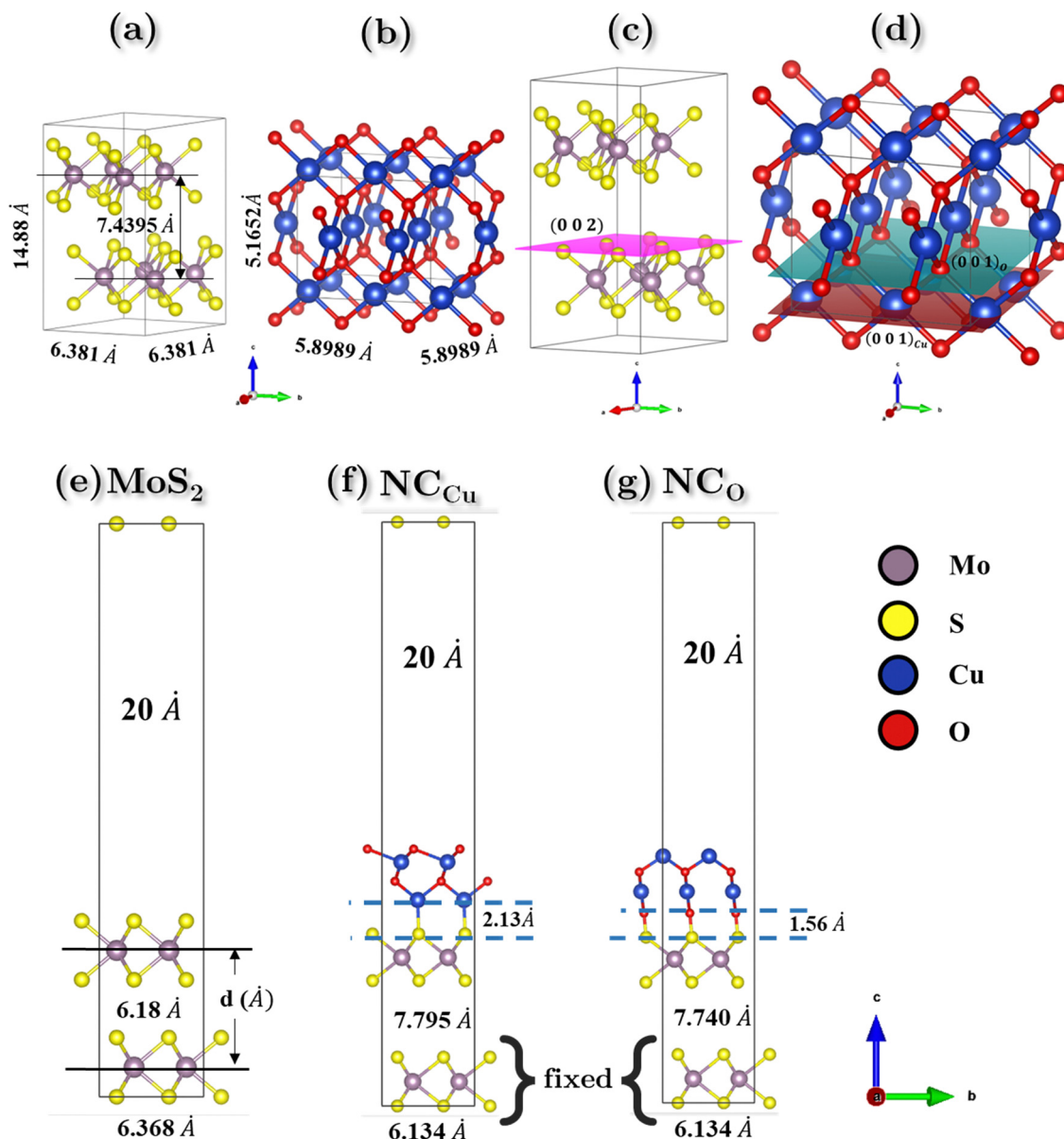
Fig. 10 Base supercell structures along with their lattice parameters for (a) bilayer MoS$_2$ and (b) CuO. Lattice planes showing predominant surface plane(s) for (c) nF-MoS$_2$ (002) and (d) nP-CuO(001) with Cu and O terminations. (e) Surface slab of MoS$_2$ and (f) and (g) interface model for the nF-MoS$_2$/nP-CuO nanocomposite with Cu (NC$_{Cu}$) and O (NC$_O$) terminations, respectively, with 20 Å of vacuum along the c direction.

accounting for van der Waals interactions, the atomic band projection, and the band projected onto the MoS$_2$ surface slab for (c) and (d) NC$_{Cu}$, (e), (f) NC$_O$ nanocomposite interfaces. Here, VBM = E_F = 0.

The analysis of atomic bands reveals that the MoS$_2$ bilayer has an indirect band gap of 1.52 and 1.17 eV, with and without dispersion correction, respectively (as depicted in Fig. 11(a) and (b)). These values are smaller than the experimental value (1.6 eV).[58] Also the valence band maximum (VBM) and conduction band minimum (CBM) are found to be predominantly composed of Mo atoms, with a minor contribution from S atoms in the case of VBM. The analysis of the projected density of states (PDOS) calculation reveals that the VBM and CBM are derived from the 4d and 4p orbitals of the Mo atoms,

respectively. The interfacial states near the Fermi level in the NC$_{Cu}$ and NC$_O$ systems are primarily composed of O-2p states, as evidenced by the TDOS and band structure illustrated in Fig. 11c, e and 12a. Notably, the interfacial states in the NC$_{Cu}$ system are dominated by O-2p orbitals. In contrast, these orbitals have minimal influence in the NC$_O$ system, as demonstrated by the projected density of states (PDOS) analysis of Mo-4d, Cu-3d, and O-2p orbitals in Fig. 12c and d. Moreover, the interfacial interactions have modified the Mo-d orbitals more for NC$_{Cu}$ than NC$_O$, shifting the orbitals to the left towards lower energy in both cases. In our experimental study, the primary component is nF-MoS$_2$, while nP-CuO is added in a minor capacity, serving solely as a modifier. MoS$_2$ predominantly governs the electronic characteristics, and the MoS$_2$–
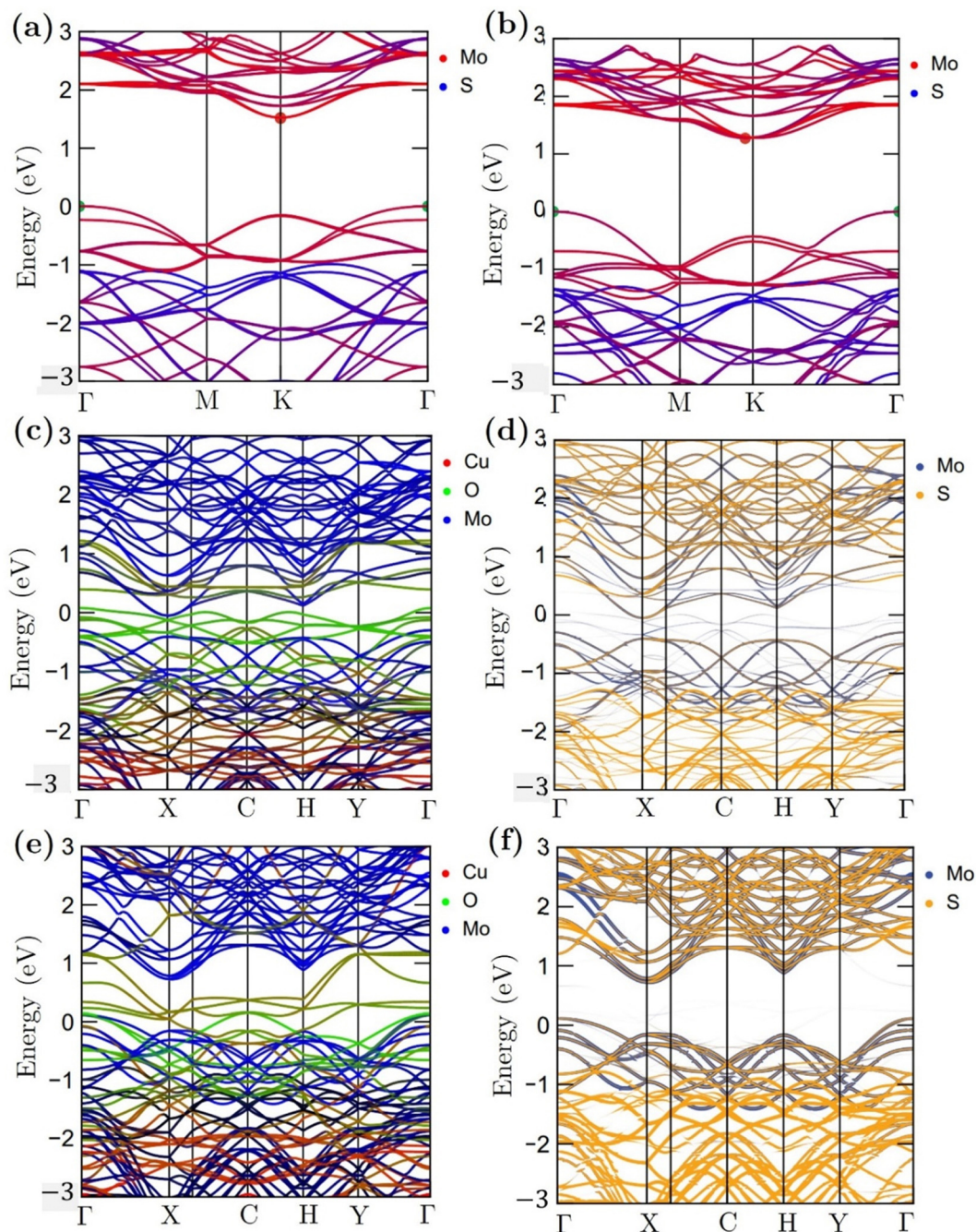
Fig. 11 Atomic band projected band structure of the MoS$_2$ surface slab with an indirect bandgap (a) with and (b) without accounting for van der Waals interactions, atomic band projection and the band projected onto the MoS$_2$ surface slab for (c) and (d) NC$_{Cu}$ and (e) and (f) NC$_O$ nanocomposite interfaces. Here, VBM = E_F = 0.

CuO interface is a critical factor in altering this basic electronic configuration. As the CuO content increases, the impact of interfacial interaction becomes more pronounced. Our findings reveal a significant impact on the band structure (as depicted in Fig. 11d and f), with the most prominent feature being a reduction in the band gap. This observation is further supported by experimental evidence. Due to a comparative abundance of O-2p states near the band gap of NC$_{Cu}$ with respect to NC$_O$, the projected band gap of NC$_{Cu}$ is smaller than that of

NC$_O$, around 0.2 eV compared to 0.9 eV. Although the calculated band gaps of MoS$_2$ and CuO (001: Cu, O) in this work were underestimated using the GGA+U functional, the relative trends between these values were still helpful in analyzing the charge-carrier transfer behavior. The hybridization between the 3p states of the modified d orbitals from Mo sites and p orbitals from O sites in the interface region helps to maintain an increased number of states near the Fermi level by reinforcing their presence, and as a result, we get two positive outcomes.
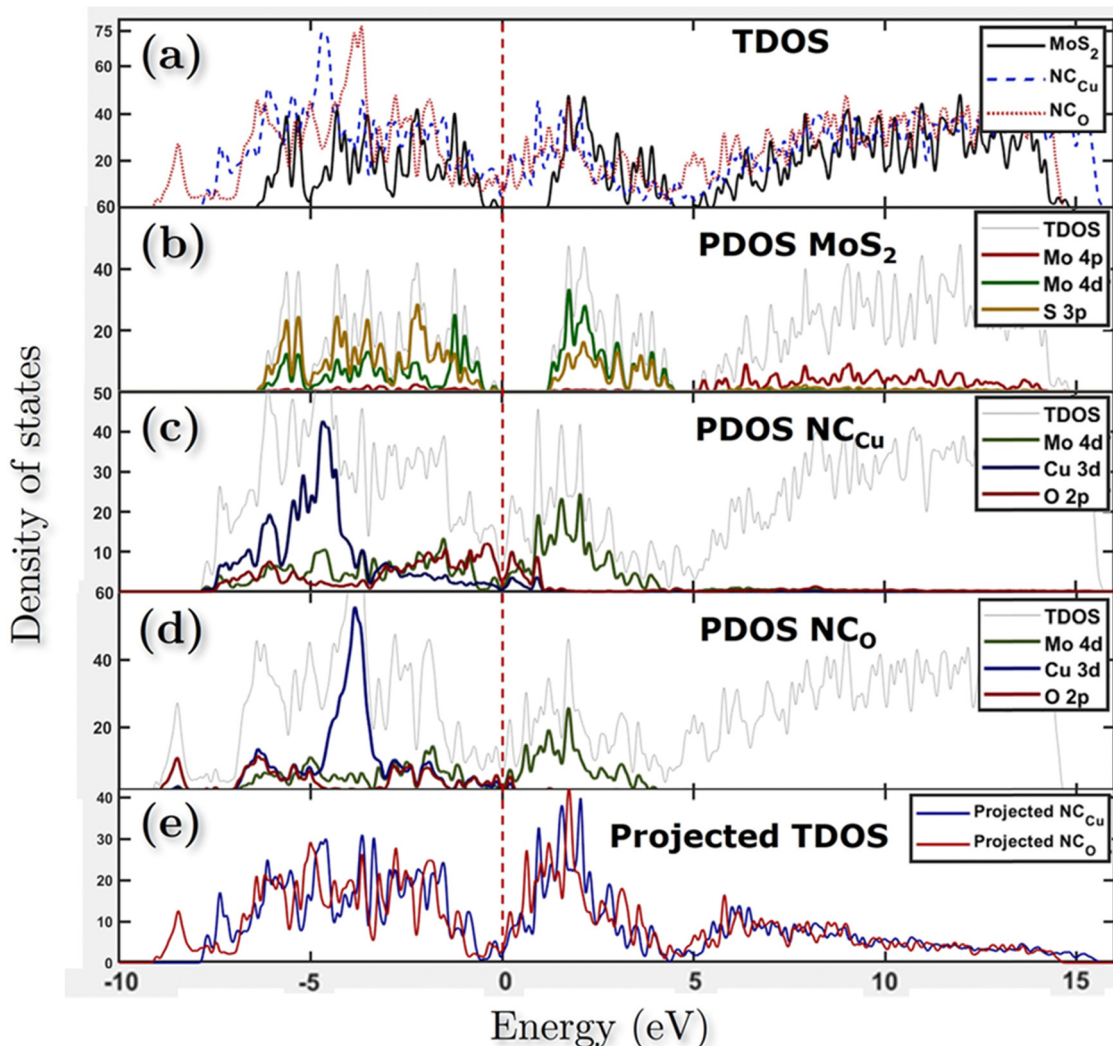
Fig. 12 (a) Total density of states (TDOS) for all models and projected density of states (PDOS) of (b) MoS_2 surface slab, (c) NC_{Cu}, (d) NC_O and (e) TDOS for both NC_{Cu} and NC_O models only projected onto the MoS_2 slab. Here, VBM = E_F = 0.

One is that the projected band gap of MoS_2 has decreased, resulting in a higher conductivity suitable for capacitance. Another outcome is that the increased states result in a higher density of available states for charge storage, as shown in the quantum capacitance calculation, resulting in an increased specific capacitance for CuO-incorporated MoS_2. The Cu-3d states are not present near the Fermi level as they reside deep inside the VBs. Another important observation from Fig. 12e is that the TDOSs have shifted towards lower energy, which is more prominent for NC_O due to a stronger interfacial dipole than NC_{Cu}.

3.8. Simulated optical properties

This study investigates the electronic transitions responsible for the optical properties observed in the surface slab of MoS_2 and in NC_{Cu} and NC_O. Fig. 13a (inset) illustrates that for a MoS_2 surface slab, the lowest energy incident photons result in the most positive value for the real part, while the imaginary part approaches zero. In contrast, the heterostructures exhibit an exponential increase in their actual value, resulting in a

significantly high positive value for low-energy photons. Additionally, the imaginary component is non-zero and comparatively greater for NC_{Cu} than for NC_O. The absorption coefficient measures the proportion of energy that a wave loses as it traverses a substance, resulting in a decrease in intensity at a distance x from the surface, as expressed by the equation:

$$I(x) = I(0)\exp(-\eta x)$$

where $I(0)$ is the incident light intensity and $\eta = \dfrac{2k\omega}{c}$ with k denoting the imaginary component of refractive index and ω representing the frequency of light. As depicted in Fig. 13b, the absorption coefficient has exhibited a reduction across the entire spectrum of photon energy for both heterostructures, resulting in a red shift towards lower energy levels compared with the MoS_2 slab. As a result of the red shift, a greater quantity of low-energy photons will be absorbed compared to the MoS_2 surface slab. As the CuO content rises, it has been noted that the optical band gap is reduced. Consequently, the nanocomposite exhibits a greater capacity for absorbing

photons with lower energy levels. The optical band gaps (Fig. 13b inset) are around 1.4 eV, 0.7 eV, and 0.9 eV for MoS_2, NC_{Cu}, and NC_O, respectively. The MoS_2/CuO nanocomposite exhibits a smaller bandgap than the pure MoS_2 nanoparticles, and the presence of intermediate states may contribute to an increase in the nanocomposite's conductivity. This enhanced conductivity may subsequently lead to a rise in the nanocomposite's capacitance.

The NC_{Cu} exhibits a reflectivity of approximately 35%, while the NC_O demonstrates a reflectivity of about 31%. These values are comparatively higher than the reflectivity of the MoS_2 surface slab, about 18%, as depicted in Fig. 13c.

Typically, the difference in transmitting an electromagnetic wave across a vacuum and other substances can be explicated by a complex refractive index. For transparent materials, this index is exclusively real. In the case of MoS_2 surface slabs and heterostructures, it can be observed that both the real and imaginary components make a significant contribution across most of the energy spectrum. In the vicinity of low photon energy, it can be observed that the refractive index of the MoS_2 surface slab is entirely real, approximately 2.5, as depicted in the inset of Fig. 13d. In both heterostructures depicted in Fig. 13d, the lower energy range exhibits comparable

characteristics to its dielectric function. Specifically, the real component of the refractive index increases exponentially, while the imaginary component remains non-zero.

3.9. Interfacial structure

Upon relaxation, the distance between the nF-MoS_2 and nP-CuO interface was determined to be 2.13 Å for NC_{Cu}. Additionally, the interlayer spacing between MoS_2 layers increased from 6.18 Å to 7.795 Å. The interfacial distance between the two heterostructures in NC_O has been observed to decrease to 1.56 Å, while the interlayer distance of MoS_2 reduces from 7.795 Å to 7.74 Å.

The calculation of the surface energy of the MoS_2 surface oriented along the (002) direction is performed through the utilization of equation in the following manner,

$$E_{surf} = E_{MoS_2-bulk} - E_{MoS_2-surface\ slab}$$

where E_{MoS_2-bulk} and $E_{MoS_2-surface\ slab}$ are the energies of bulk-, and a surface slab of MoS_2, respectively.

To assess the interfacial stability of the composites quantitatively, the interfacial interaction energy (E_{int}) was calculated using the formula

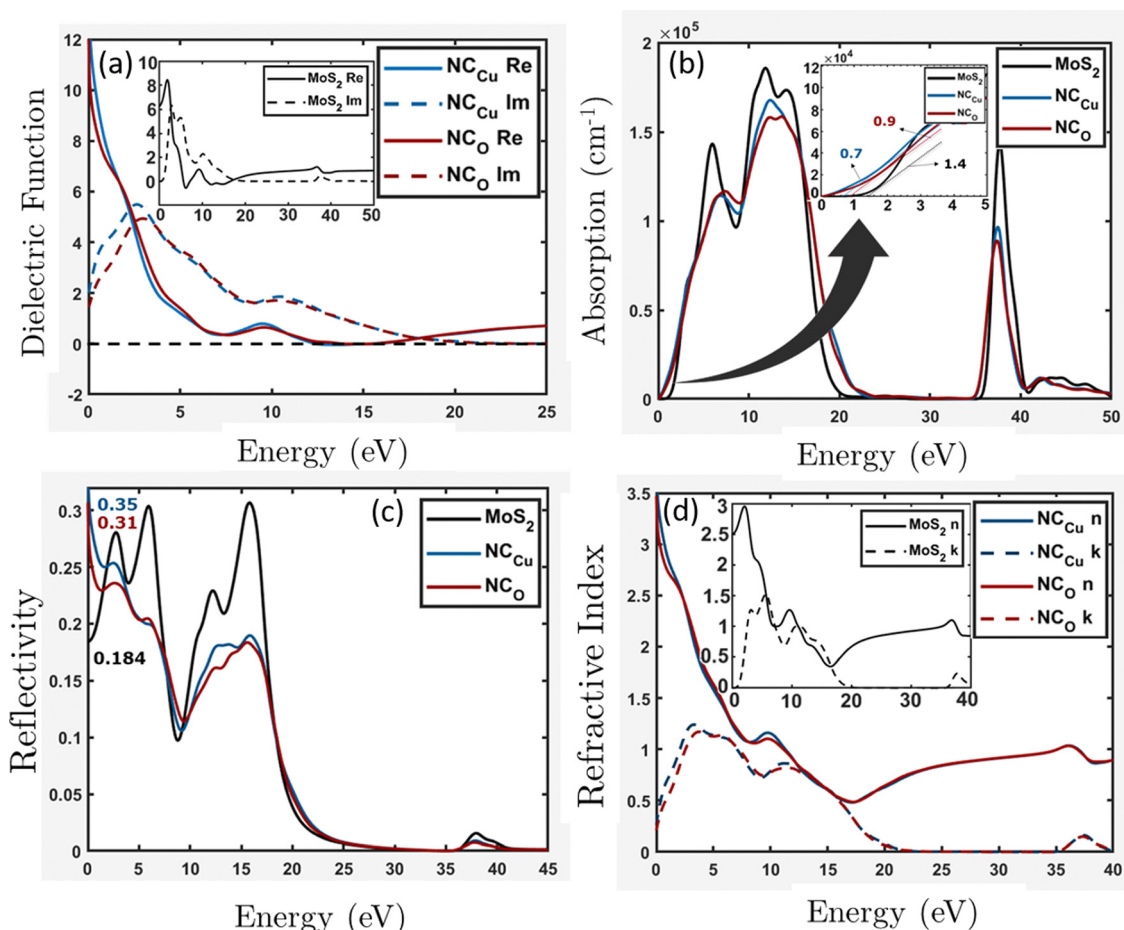$$E_{int} = E_{MoS_2-CuO(Cu:O)} - E_{MoS_2} - E_{CuO}$$

Fig. 13 Optical properties (a) dielectric function, (b) absorption, (c) reflectivity and (d) refractive index for the MoS_2 surface slab, NC_{Cu} and NC_O.

where $E_{MoS_2-CuO(Cu:O)}$, E_{MoS_2}, and E_{CuO} are the energies of the composite for both terminations, bilayer MoS_2 and CuO. A higher degree of stability of the interface (surface) is indicated by a more negative value of the obtained E_{int}. Additionally, the interfacial stability of the nanocomposites was evaluated by utilizing the work of adhesion (W_{ad}). The term W_{ad} refers to the interfacial bonding energy required to separate the interface into two surfaces reversibly, as expressed in the following equation

$$W_{ad} = \frac{E_{MoS_2} + E_{CuO} - E_{MoS_2-CuO(Cu:O)}}{A} = -\frac{E_{int(surf)}}{A}$$

The variable $E_{int(surf)}$ represents the interfacial (surface) interaction energy, expressed as a negative value, and A denotes the interfacial area.

Table 7 indicates that the surface and interfacial energies exhibit negative values, signifying stability. Notably, NC_{Cu} demonstrates the most stable configuration, with an interfacial interaction energy of -4.8 eV, the lowest among the observed values. In terms of both interfacial distances and energetics, NC_{Cu} aligns more closely with experimental findings. The experimentally observed interfacial distance is around 2.54 Å, similar to our calculated value of 2.13 Å, and the inter-layer distance between MoS_2 layers has increased in both cases.[62] Moreover, according to previous research, adsorption distances between 2.0 Å and 2.5 Å indicate chemical interactions.[65] Based on this criterion, all the studied systems exhibit chemisorption behavior. This strong interaction between MoS_2 and CuO can prevent other MoS_2 layers from sticking to themselves, resulting in a more exposed active surface area.

To gain insight into the bond properties of the suggested models, a Mulliken bond population computation was carried out. Sanchez-Portal *et al.* have proposed a method for population analysis, which involves projecting the plane wave (PW) states onto a localized basis.[67] Subsequently, the studied states are analyzed using a Mulliken formalism-based population approach.[68] The utilization of the overlap population can help in determining whether a bond is covalent or ionic. A high population is indicative of a covalent bond, while a low bond population value is indicative of an ionic contact. The findings presented in Table 7 suggest a decreasing trend in the covalence of the Mo–S bond for the MoS_2 layer in proximity to the interface exhibits, with the MoS_2 surface slab demonstrating the highest covalence, followed by NC_{Cu} and NC_O. Regarding NC_{Cu} and NC_O heterostructures, the Cu–O bond exhibits a higher degree of ionic character than the Cu–S bond. Additionally, a comparison between the two heterostructures reveals

that the Cu–O bond in NC_{Cu} displays a greater level of covalency than that in NC_O.

3.10. Redistribution of charge

To offer quantitative depictions of the charge distributions, it is advantageous to partition the system into distinct atomic fragments. As defined by Hirshfeld charge,[69] the deformation density is the distinguishing factor between molecular and unrelaxed atomic charge densities. A general approach is to distribute the charge density among the atoms at every location in a manner that corresponds to their respective free-atom densities at the corresponding distances from the nucleus. The aforementioned prescription results in bonded-atom distributions that are highly localized and exhibit a close resemblance to the molecular density in their respective vicinity. The definition of the charge on atom A, q_A, is given using the following equation:

$$q_A = Z_A - \int dr \frac{\rho_A^0(r)}{\sum_B \rho_B^0(r)} \rho(r)$$

The equation mentioned above pertains to the nuclear charge of element A, denoted as Z_A, the isolated ground-state atomic density of element B, represented as ρ_B^0, and the molecular density, characterized as ρ. The Hirshfeld charges are prone to underestimation when compared to empirical data. As per the Hirshfeld charge analysis, it can be observed that the atom-centered negative charge on the sulfur atoms of the MoS_2 layer for both heterostructures (Fig. 14b and c) has decreased compared to the MoS_2 surface slab (Fig. 14a).

This decrease in the negative charge on the S atoms means they are less polarizable. As we know, van der Waals force is proportional to the polarizability of the molecules, and so more polarizable molecules will experience a stronger van der Waals force. The observed expansion of interlayer spacing in the MoS_2 bilayer can be attributed to a reduction in the van der Waals attractive force. The disparity in charge between interfacial O–S atoms in NC_O is more pronounced than that between Cu–S atoms in NC_{Cu}. This leads to the inference that the charges in NC_{Cu} are centered on the bond, whereas NCO charges are centered on the atom. This distinction will be further elucidated in the subsequent analysis of the charge density difference.

To gain a deeper understanding of the electronic structure evolution resulting from interfacial interaction, the charge density differences were computed (as depicted in Fig. 14). The definition of the charge density difference was established as presented in eqn (1),

Table 7 Interfacial (surface) interaction energy, bonding energy, interlayer distance between MoS_2 bilayers and average Mulliken bond population of Mo–S, Cu–S, O–S and Cu–O bonds situated at surface (interface) sites for the MoS_2 surface slab (two layers) and interfacial models with Cu and O terminations of CuO

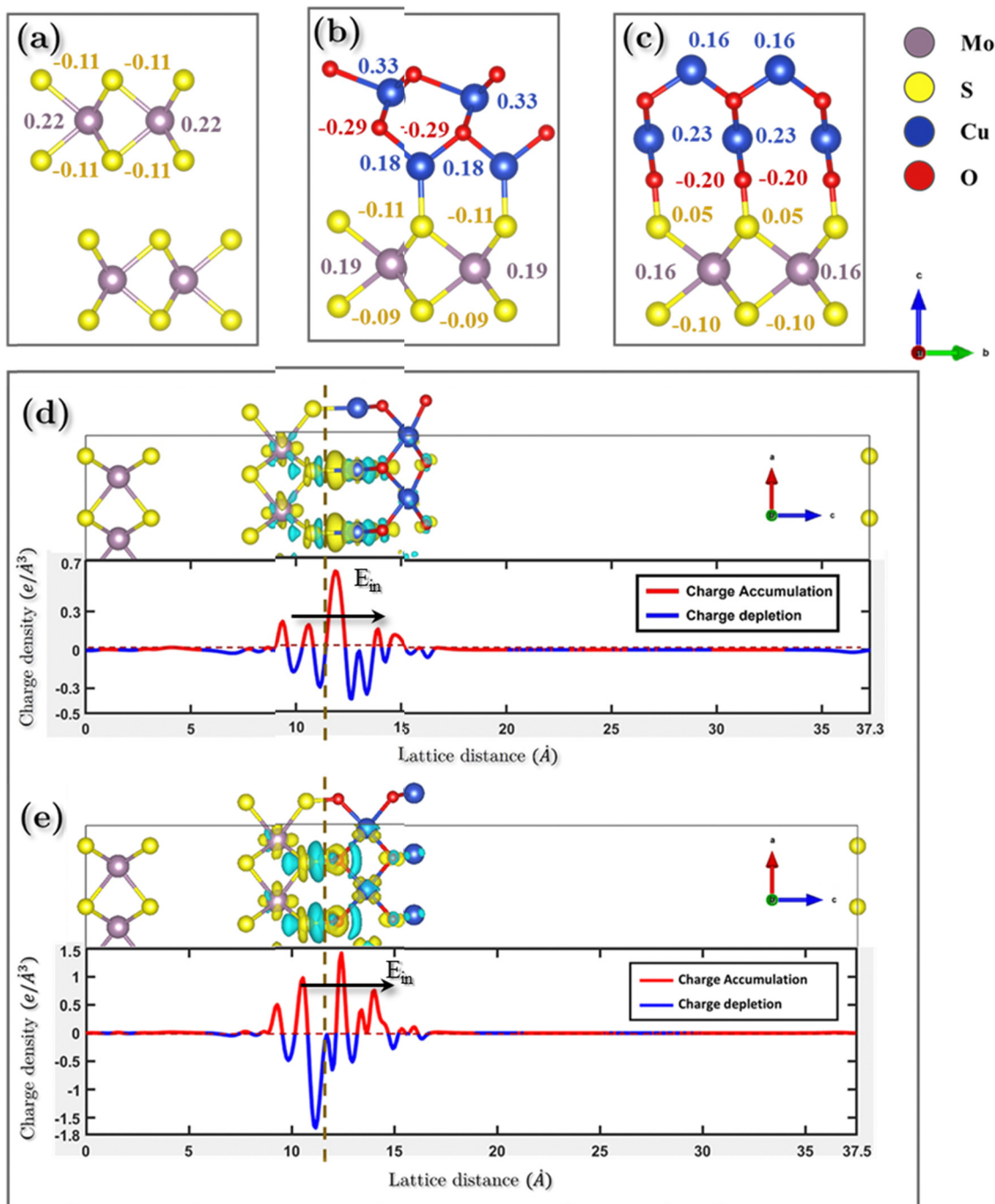| Materials	$E_{int(surf)}$ (eV)	W_{ad} (J m^{-2})	MoS_2 interlayer distance d (Å)			Average bond population			
			Exp.[62]	Theor.[66]	This work	Mo–S	Cu–S	O–S	Cu–O
MoS_2	-1.1	0.026	6.2	7.88	6.18	0.435	NA		
NC_{Cu}	-4.8	0.127	6.22	NA	7.79	0.403	0.530	NA	0.41
NC_O	-0.88	0.023			7.74	0.370	NA	0.390	0.305

Fig. 14 Atomic charge distributions using Hirshfeld charge analysis for (a) MoS$_2$ surface slab, (b) NC$_{Cu}$ and (c) NC$_O$. Charge density differences (3D plot, yellow = charge accumulation and blue = charge depletion) and average charge density differences (line plot) of (d) NC$_{Cu}$ and (e) NC$_O$.

$$\Delta\rho_{\text{difference}} = \rho_{\text{total}} - \Sigma\rho_i \qquad (1)$$

where ρ_i and ρ_{total} are the charge density of the crystal slab and total charge density of the nanocomposite, respectively. The variation in density indicates the transfer of interfacial charges from MoS$_2$ to CuO in the heterostructures (*e.g.*, Fig. 14d and e).

The phenomenon of charge separation is observed to be more pronounced in the NC$_O$ model as compared to NC$_{Cu}$. This is attributed to the formation of strong S–O chemical bonds at

the interface of the NC$_O$ model, which serves as a significant driving force for facilitating the transfer of charges. The observed phenomenon entailed a reduction in electron density oscillation from the MoS$_2$–CuO interface. Regarding NC$_{Cu}$, the redistribution of charges is confined to the interfacial vacuum region, in contrast to the previous scenario where the charge redistribution was primarily concentrated on the Cu–S bond. Moreover, the charge redistribution is concentrated mainly in the interfacial region between the first layer of the MoS$_2$, which

is consistent with the fact that gap states are mainly present in the first layer of MoS$_2$. In other words, gap states do not significantly penetrate into the "bulk" region of MoS$_2$. Upon closer examination, it is observed that the electrons on the CuO side extend about 0.87 Å and 2.2 Å for NC$_{Cu}$ and NC$_O$, respectively, while the positive charges on the MoS$_2$ side extend about 3 Å for NC$_{Cu}$ and 3.22 Å for NC$_O$, respectively. Overall, the electrons extend over a shorter distance in the CuO region compared to MoS$_2$. This can be attributed to the high electron density of CuO.

The transfer of net charge from the MoS$_2$ slab to the CuO monolayer yields a significant inherent built-in electric field (E_{in}) that extends from MoS$_2$ to CuO. The significant electric field that is inherently present facilitates the movement of electrons from CuO toward MoS$_2$, thereby enhancing the interlayer coupling. The phenomenon of charge density attraction between MoS$_2$ and CuO is believed to play a significant role in augmenting the charge storage capacity of the composite.

3.11. Quantum capacitance

To elucidate the increased specific capacitance due to the incorporation of CuO, we performed calculations to determine the quantum capacitance (C_Q) of pure MoS$_2$ and CuO incorporated nanocomposites utilizing the DOS of MoS$_2$ and MoS$_2$/CuO nanocomposites. The concept of quantum capacitance refers to the manner in which excessive charges, specifically ions, respond to a change in applied potential and is measured as the rate of this change.[70] The expression for the derivative of the net charge on the substrate or electrode with respect to electrostatic potential can be formulated as follows,

$$C_Q = \frac{dQ}{d\phi}$$

where Q is the electrode's excessive charge and ϕ is the chemical potential. The overall electric charge is directly proportional to the weighted summation of the electronic states' density up to the Fermi energy level E_F. This charge can be expressed as an integral involving the electronic density of state $D(E)$ and the Fermi–Dirac distribution function $f(E)$ as follows:

$$Q = e \int_{-\infty}^{+\infty} D(E)[f(E) - f(E - \phi)]dE$$

Hence, it is possible to compute the quantum capacitance (C_Q) of a channel at a non-zero temperature T by utilizing the density of states (DOS) as,

$$C_Q = \frac{dQ}{d\phi} = \frac{e^2}{4kT} \int_{-\infty}^{+\infty} D(E)\,\mathrm{sech}^2\left(\frac{E - e\phi}{2kT}\right)dE \quad (2)$$

The aforementioned equation involves the charge of electrons denoted by e, the chemical potential represented by ϕ, the density of states (DOS) indicated by $D(E)$, and the Boltzmann constant represented by k. Thus, the computation of the charge quantization for the entire system has been approximated solely based on the density of states. The study employed a potential window ranging from -0.5 to 0.5 V, which was

determined based on the established limit of MoS$_2$ capacitance in aqueous electrolytes, as reported in the literature.[71]

From Fig. 15, it can be observed that NC$_{Cu}$ and NC$_O$ show C_Q values of around 401.3 and 302.1 F g^{-1} near the Fermi level ($E_F = 0$), representing an increase of around 6.6-fold and 5-fold, respectively, compared to pure MoS$_2$, which has a C_Q value of around 61.01 F g^{-1}. These values are comparable to our experimental calculation of specific capacitance shown in Table 3. The highest specific capacitance was found for 4 wt% CuO incorporation with a value of 336.23 F g^{-1}, which is 5.8-fold greater than that of pure MoS$_2$, which shows a specific capacitance value of 58.07 F g^{-1}. This trend is consistent with theoretical calculations.

Eqn (2) presents the formulation of C_Q, indicating that the quantum capacitance exhibits a direct correlation with the density of states in the vicinity of the Fermi energy. The contribution of states that are energetically distant from the Fermi level is negligible. This is because the energy relative to the Fermi level is represented by $(E - e\phi)$, and the function $\mathrm{sech}^2(x)$ approaches zero rapidly for $|x| > 0$. The increased capacitance observed in CuO-incorporated MoS$_2$ nanocomposites can be attributed to the amplified density of states near the Fermi level. The origin of these states has been discussed in the electronic properties section.

In summary, the hybrid experimental and computational study has demonstrated that the inclusion of CuO has resulted in an augmentation of the charge storage capacity and specific capacitance of MoS$_2$ for various reasons. (1) CuO slices possessing a layered structure with {001} planes have the potential to demonstrate super capacitance behavior independently. (2) MoS$_2$ nanosheets can function as a substrate to uniformly hold CuO nanoparticles, thereby preventing their agglomeration. (3) Likewise, introducing CuO slices can prevent the restacking of MoS$_2$ nanosheets. (4) Using modified MoS$_2$ nanosheets results in a considerably greater active surface area. (5) The inclusion
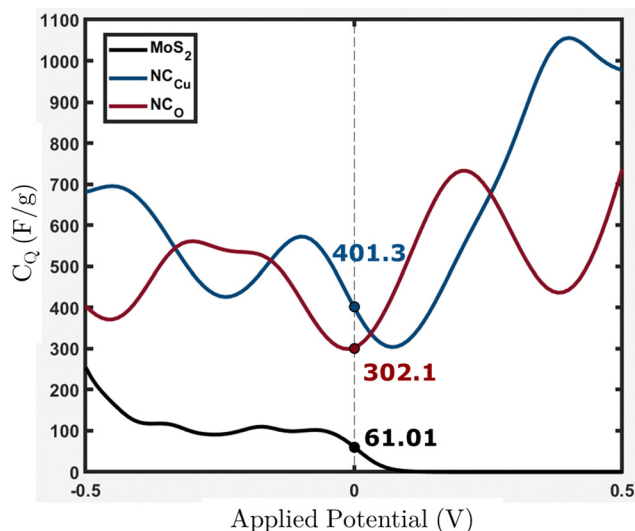

Fig. 15 Calculated quantum capacitance (C_Q) for the MoS$_2$ surface slab, NC$_{Cu}$ and NC$_O$ with values near $E_F = 0$.

of CuO would lead to the generation of numerous energy levels in proximity to the Fermi level. The collective impact of these factors can enhance the specific capacitance of MoS_2 nanoflowers synergistically.

4. Conclusion

In brief, a hydrothermal synthesis method was employed to fabricate MoS_2/CuO composite nanomaterials with varying concentrations of CuO nanoparticles. The electrochemical investigation revealed that the inclusion of CuO nanoparticles resulted in a noteworthy enhancement of the electrochemical efficacy of MoS_2/CuO nanocomposites. The study showed that the MoS_2/CuO(4%) composite material demonstrated a specific capacitance of 336.23 F g^{-1} and an energy density of 24.99 W h kg^{-1} when subjected to a current density of 0.1 A g^{-1}. Furthermore, the specimen demonstrates exceptional cyclic stability, evidenced by its capacitive retention rate of 89.7% even after 4000 cycles. From a structural, morphological standpoint, the theoretical calculations suggest that the incorporation of CuO nanoparticles can prevent the restacking of MoS_2 layers due to their assertive chemisorption behavior, thus increasing the active surface area for the intercalation of charges and ions. The hybridization in the interface region between Mo and O orbitals leads to an increase in states near the Fermi level, resulting in higher conductivity and specific capacitance for MoS_2 with CuO incorporation. Due to these states, we see a decreasing trend in the optical band gap from absorbance calculations, resulting in higher conductivity. Moreover, the quantum capacitance calculations demonstrate that these newly generated states can accommodate more charge. The charge transfer from MoS_2 to CuO results in a strong intrinsic electric field that improves electron transfer and creates a longer path for the charges. As a result, the charging and discharging processes take longer, resulting in increased specific capacitance of MoS_2. Thus, the presented experimental and theoretical evidence indicates that the inclusion of CuO into MoS_2 yields a beneficial synergistic outcome, leading to a promising material that can effectively compete in advanced energy storage applications.

Conflicts of interest

There are no conflicts to declare.

Acknowledgements

References

1 J. Zhan, G. Li, Q. Gu, H. Wu, L. Su and L. Wang, Porous Carbon Nanosheets Armoring 3D Current Collectors toward Ultrahigh Mass Loading for High-Energy-Density All-Solid-State Supercapacitors, *ACS Appl. Mater. Interfaces*, 2021, **13**(44), 52519–52529.

2 J. R. Miller and P. Simon, Electrochemical capacitors for energy management, *Science*, 2008, **321**(5889), 651–652.

3 X. Wang, T. Wang, R. Zhou, L. Fan, S. Zhang, F. Yu, T. Tesfamichael, L. Su and H. Wang, Ultrathin $Ni_{1-x}Co_xS_2$ nanoflakes as high energy density electrode materials for asymmetric supercapacitors, *Beilstein J. Nanotechnol.*, 2019, **10**(1), 2207–2216.

4 Z. Wu, G. Tai, X. Wang, T. Hu, R. Wang and W. Guo, Large-area synthesis and photoelectric properties of few-layer $MoSe_2$ on molybdenum foils, *Nanotechnology*, 2018, **29**(12), 125605.

5 X. Huang, Z. Zeng and H. Zhang, Metal dichalcogenide nanosheets: preparation, properties and applications, *Chem. Soc. Rev.*, 2013, **42**(5), 1934–1946.

6 G. Tai, T. Zeng, J. Yu, J. Zhou, Y. You, X. Wang, H. Wu, X. Sun, T. Hu and W. Guo, Fast and large-area growth of uniform MoS_2 monolayers on molybdenum foils, *Nanoscale*, 2016, **8**(4), 2234–2241.

7 X. Wang, G. Tai, Z. Wu, T. Hu and R. Wang, Ultrathin molybdenum boride films for highly efficient catalysis of the hydrogen evolution reaction, *J. Mater. Chem. A*, 2017, **5**(45), 23471–23475.

8 H. Gómez, M. K. Ram, F. Alvi, P. Villalba, E. L. Stefanakos and A. Kumar, Graphene-conducting polymer nanocomposite as novel electrode for supercapacitors, *J. Power Sources*, 2011, **196**(8), 4102–4108.

9 L. Fang, Z. Zhang, X. Li, H. Zhou, K. Ma, L. Ge and K. Huang, Fabrication of hybrid cauliflower-like nanoarchitectures by in situ grown ZnO nanoparticals on VS_2 ultrathin nanosheets for high performance supercapacitors, *Colloids Surf., A*, 2016, **501**, 42–48.

10 X. Wang, T. Wang, L. Su, T. Tesfamichael, F. Yu, Z. Shi and H. Wang, Synthesis of $Co_xNi_{1-x}S_2$ electrode material with a greatly enhanced electrochemical performance for supercapacitors by *in situ* solid-state transformation, *J. Alloys Compd.*, 2019, **803**, 950–957.

11 M. Xu, R. Wang, K. Bian, C. Hou, Y. Wu and G. Tai, Triclinic boron nanosheets high-efficient electrocatalysts for water splitting, *Nanotechnology*, 2021, **33**(7), 075601.

12 J. Zhou, M. Guo, L. Wang, Y. Ding, Z. Zhang, Y. Tang, C. Liu and S. Luo, 1T-MoS_2 nanosheets confined among TiO_2 nanotube arrays for high performance supercapacitor, *Chem. Eng. J.*, 2019, **366**, 163–171.

13 H. Zhang, J. Wei, Y. Yan, Q. Guo, L. Xie, Z. Yang, J. He, W. Qi, Z. Cao, X. Zhao and P. Pan, Facile and scalable fabrication of MnO_2 nanocrystallines and enhanced electrochemical performance of MnO_2/MoS_2 inner heterojunction structure for supercapacitor application, *J. Power Sources*, 2020, **450**, 227616.

14 M. H. Ahmad, R. B. Alam, A. Ul-Hamid, S. F. U. Farhad and M. R. Islam, Hydrothermal synthesis of Co_3O_4 nanoparticles

decorated three dimensional MoS_2 nanoflower for exceptionally stable supercapacitor electrode with improved capacitive performance, *J. Energy Storage*, 2022, **47**, 103551.

15 M. Wang, H. Fei, P. Zhang and L. Yin, Hierarchically layered MoS_2/Mn_3O_4 hybrid architectures for electrochemical supercapacitors with enhanced performance, *Electrochim. Acta*, 2016, **209**, 389–398.

16 K. Chanda, S. Thakur, S. Maiti, A. Acharya, T. Paul, N. Besra, S. Sarkar, A. Das, K. Sardar and K. K. Chattopadhyay, Hierarchical heterostructure of MoS_2 flake anchored on TiO_2 sphere for supercapacitor application, *AIP Conf.: Proc.*, 2018, **1953**(1), 030138 (AIP Publishing LLC).

17 S. E. Moosavifard, M. F. El-Kady, M. S. Rahmanifar, R. B. Kaner and M. F. Mousavi, Designing 3D highly ordered nanoporous CuO electrodes for high-performance asymmetric supercapacitors, *ACS Appl. Mater. Interfaces*, 2015, **7**(8), 4851–4860.

18 K. K. Purushothaman, B. Saravanakumar, I. M. Babu, B. Sethuraman and G. Muralidharan, Nanostructured CuO/reduced graphene oxide composite for hybrid supercapacitors, *RSC Adv.*, 2014, **4**(45), 23485–23491.

19 G. P. Awasthi, M. B. Poudel, M. Shin, K. P. Sharma, H. J. Kim and C. Yu, Facile synthesis of a copper oxide/molybdenum disulfide heterostructure for asymmetric supercapacitors of high specific energy, *J. Energy Storage*, 2021, **42**, 103140.

20 X. Ge, C. Klingshirn, M. Morales, M. Wuttig, O. Rabin, S. Zhang and L. G. Salamanca-Riba, Electrical and structural characterization of nano-carbon–aluminum composites fabricated by electro-charging-assisted process, *Carbon*, 2021, **173**, 115–125.

21 M. R. Islam, J. E. Obaid, M. Saiduzzaman, S. S. Nishat, T. Debnath and A. Kabir, Effect of Al doping on the structural and optical properties of CuO nanoparticles prepared by solution combustion method: experiment and DFT investigation, *J. Phys. Chem. Solids*, 2020, **147**, 109646.

22 J. Hafner and G. Kresse, The vienna ab-initio simulation program VASP: an efficient and versatile tool for studying the structural, dynamic, and electronic properties of materials, *Properties Complex Inorganic Solids*, 1997, **140**, 69–82.

23 G. Kresse and D. Joubert, From ultrasoft pseudopotentials to the projector augmented-wave method, *Phys. Rev. B: Condens. Matter Mater. Phys.*, 1999, **59**(3), 1758.

24 P. E. Blöchl, Projector augmented-wave method, *Phys. Rev. B: Condens. Matter Mater. Phys.*, 1994, **50**(24), 17953.

25 G. Kresse and J. Furthmüller, Efficient iterative schemes for ab initio total-energy calculations using a plane-wave basis set, *Phys. Rev. B: Condens. Matter Mater. Phys.*, 1996, **54**(16), 11169.

26 V. I. Anisimov, J. Zaanen and O. K. Andersen, Band theory and Mott insulators: Hubbard U instead of Stoner I, *Phys. Rev. B: Condens. Matter Mater. Phys.*, 1991, **44**(3), 943.

27 H. Hsu, P. Blaha, R. M. Wentzcovitch and C. Leighton, Cobalt spin states and hyperfine interactions in $LaCoO_3$ investigated by LDA+U calculations, *Phys. Rev. B: Condens. Matter Mater. Phys.*, 2010, **82**(10), 100406.

28 M. R. Akhond and A. Sharif, Role of hydrogen co-doping on opto-electronic behaviors of Na–H co-doped zinc oxide: a first principle study, *J. Phys. Commun.*, 2020, **4**(11), 115002.

29 A. V. Krukau, O. A. Vydrov, A. F. Izmaylov and G. E. Scuseria, Influence of the exchange screening parameter on the performance of screened hybrid functionals, *J. Chem. Phys.*, 2006, **125**(22), 224106.

30 F. Aryasetiawan and O. Gunnarsson, The GW method, *Rep. Prog. Phys.*, 1998, **61**(3), 237.

31 A. H. Biby, B. A. Ali and N. K. Allam, Interplay of quantum capacitance with van der Waals forces, intercalation, co-intercalation, and the number of MoS_2 layers, *Mater. Today Energy*, 2021, **20**, 100677.

32 J. P. Perdew, K. Burke and M. Ernzerhof, Generalized gradient approximation made simple, *Phys. Rev. Lett.*, 1996, **77**(18), 3865.

33 M. R. Islam, M. Saiduzzaman, S. S. Nishat, A. Kabir and S. F. U. Farhad, Synthesis, characterization and visible light-responsive photocatalysis properties of Ce doped CuO nanoparticles: a combined experimental and DFT+U study, *Colloids Surf., A*, 2021, **617**, 126386.

34 B. Abebe, H. A. Murthy, E. A. Zereffa and Y. Qiang, Synthesis and characterization of PVA-assisted metal oxide nanomaterials: surface area, porosity, and electrochemical property improvement, *J. Nanomater.*, 2020, **2020**, 1–14.

35 L. Hu, Y. Ren, H. Yang and Q. Xu, Fabrication of 3D hierarchical MoS_2/polyaniline and MoS_2/C architectures for lithium-ion battery applications, *ACS Appl. Mater. Interfaces*, 2014, **6**(16), 14644–14652.

36 X. Ding, Y. Huang, S. Li, N. Zhang and J. Wang, 3D architecture reduced graphene oxide-MoS_2 composite: preparation and excellent electromagnetic wave absorption performance, *Composites, Part A*, 2016, **90**, 424–432.

37 M. Chen, Y. Dai, J. Wang, Q. Wang, Y. Wang, X. Cheng and X. Yan, Smart combination of three-dimensional-flower-like MoS_2 nanospheres/interconnected carbon nanotubes for application in supercapacitor with enhanced electrochemical performance, *J. Alloys Compd.*, 2017, **696**, 900–906.

38 S. Dutta and S. De, MoS_2 nanosheet/rGO hybrid: an electrode material for high performance thin film supercapacitor, *Mater. Today: Proc.*, 2018, **5**(3), 9771–9775.

39 N. Kumar, P. Siroha, H. Shankar, D. Singh, Y. Sharma, R. Kumar, N. Yadav, K. K. Dey, H. Borkar and J. Gangwar, Probing into crystallography and morphology properties of MoS_2 nanoflowers synthesized via temperature dependent hydrothermal method, *Nano Express*, 2022, **3**(3), 035001.

40 V. Radmilovic, H. A. Gasteiger and P. N. Ross, Structure and chemical composition of a supported Pt-Ru electrocatalyst for methanol oxidation, *J. Catal.*, 1995, **154**(1), 98–106.

41 W. S. Hummers Jr and R. E. Offeman, Preparation of graphitic oxide, *J. Am. Chem. Soc.*, 1958, **80**(6), 1339.

42 H. Y. Chien, P. C. Kuo, H. L. Kao, J. S. Chen, M. R. Chen, L. S. Lu, W. C. Chueh and W. H. Chang, Low temperature deposition of high quality single crystalline AlN thin films on sapphire using highly oriented monolayer MoS_2 as a buffer layer, *J. Cryst. Grow.*, 2020, **544**, 125726.

43 B. Han and Y. H. Hu, MoS_2 as a co-catalyst for photocatalytic hydrogen production from water, *Energy Sci. Eng.*, 2016, **4**(5), 285–304.

44 H. Zhang, W. Zhou, Z. Yang, S. Wu, F. Ouyang and H. Xu, A first-principles study of impurity effects on monolayer MoS_2: bandgap dominated by donor impurities, *Mater. Res. Express*, 2017, **4**(12), 126301.

45 Y. Gogotsi and R. M. Penner, Energy storage in nanomaterials–capacitive, pseudocapacitive, or battery-like?, *ACS Nano*, 2018, **12**(3), 2081–2083.

46 Z. Wu, B. Li, Y. Xue, J. Li, Y. Zhang and F. Gao, Fabrication of defect-rich MoS_2 ultrathin nanosheets for application in lithium-ion batteries and supercapacitors, *J. Mater. Chem. A*, 2015, **3**(38), 19445–19454.

47 R. Yadav, P. Joshi, M. Hara, T. Yana, S. Hashimoto and M. Yoshimura, Intercorrelation between physical and electrochemical behavior of nitrogen-doping in graphene for symmetric supercapacitor electrode, *SN Appl. Sci.*, 2020, **2**, 1–13.

48 G. P. Awasthi, M. B. Poudel, M. Shin, K. P. Sharma, H. J. Kim and C. Yu, Facile synthesis of a copper oxide/molybdenum disulfide heterostructure for asymmetric supercapacitors of high specific energy, *J. Energy Storage*, 2021, **42**, 103140.

49 M. R. Islam, S. N. S. Pias, R. B. Alam and S. I. Khondaker, Enhanced electrochemical performance of solution-processed single-wall carbon nanotube reinforced polyvinyl alcohol nanocomposite synthesized via solution-cast method, *Nano Express*, 2020, **1**(3), 030013.

50 L. Yang, Q. Li, Y. Wang, Y. Chen, X. Guo, Z. Wu, G. Chen, B. Zhong, W. Xiang and Y. Zhong, A review of cathode materials in lithium-sulfur batteries, *Ionics*, 2020, **26**, 5299–5318.

51 R. Ye, J. Bell, D. Patino, K. Ahmed, M. Ozkan and C. S. Ozkan, Advanced sulfur-silicon full cell architecture for lithium ion batteries, *Sci. Rep.*, 2017, **7**(1), 17264.

52 L. Q. Fan, G. J. Liu, C. Y. Zhang, J. H. Wu and Y. L. Wei, Facile one-step hydrothermal preparation of molybdenum disulfide/carbon composite for use in supercapacitor, *Int. J. Hydrogen Energy*, 2015, **40**(32), 10150–10157.

53 R. N. A. R. Seman and M. A. Azam, Hybrid heterostructures of graphene and molybdenum disulfide: the structural characterization and its supercapacitive performance in 6 M KOH electrolyte, *J. Sci.: Adv. Mater. Dev.*, 2020, **5**(4), 554–559.

54 L. Wang, Y. Ma, M. Yang and Y. Qi, Titanium plate supported MoS_2 nanosheet arrays for supercapacitor application, *Appl. Surf. Sci.*, 2017, **396**, 1466–1471.

55 X. Yang, L. Zhao and J. Lian, Arrays of hierarchical nickel sulfides/MoS_2 nanosheets supported on carbon nanotubes backbone as advanced anode materials for asymmetric supercapacitor, *J. Power Sources*, 2017, **343**, 373–382.

56 L. Wang, Y. Ma, M. Yang and Y. Qi, One-pot synthesis of 3D flower-like heterostructured SnS_2/MoS_2 for enhanced supercapacitor behavior, *RSC Adv.*, 2015, **5**(108), 89069–89075.

57 S. Ali, T. Khan, M. Khan, R. Khan and S. Hussain, Morphological structural and energy storage based study of MoS_2/ZnO nanocomposite, *Mater. Res. Express*, 2019, **6**(12), 125087.

58 R. Wisesa, *Analisis sifat termoelektrik dari monolayer transition metal dichalcogenide mox2 (x = s, se, te) dengan metode density functional theory*, Bachelor's thesis, Perpustakaan Fakultas Sains dan Teknologi UIN Jakarta.

59 B. Sheng, J. Liu, Z. Li, M. Wang, K. Zhu, J. Qiu and J. Wang, Effects of excess sulfur source on the formation and photocatalytic properties of flower-like MoS_2 spheres by hydrothermal synthesis, *Mater. Lett.*, 2015, **144**, 153–156.

60 A. K. Mishra, A. Roldan and N. H. de Leeuw, CuO surfaces and CO_2 activation: a dispersion-corrected DFT+U study, *J. Phys. Chem. C*, 2016, **120**(4), 2198–2214.

61 K. Zhou, R. Wang, B. Xu and Y. Li, Synthesis, characterization and catalytic properties of CuO nanocrystals with various shapes, *Nanotechnology*, 2006, **17**(15), 3939.

62 Y. Wang, X. Tang, Z. Liu, Z. Liu, Y. Yan, B. Yang and Z. Zhu, Fabrication of a Z-scheme MoS_2/CuO heterojunction for enhanced 2-mercaptobenzothiazole degradation activity and mechanism insight, *New J. Chem.*, 2020, **44**(42), 18264–18273.

63 A. Zur and T. C. McGill, Lattice match: an application to heteroepitaxy, *J. Appl. Phys.*, 1984, **55**(2), 378–386.

64 G. Di Liberto, Á. Morales-García and S. T. Bromley, An unconstrained approach to systematic structural and energetic screening of materials interfaces, *Nat. Commun.*, 2022, **13**(1), 6236.

65 S. Bagchi, C. Ke and H. B. Chew, Oxidation effect on the shear strength of graphene on aluminum and titanium surfaces, *Phys. Rev. B*, 2018, **98**(17), 174106.

66 J. Xiao, M. Long, X. Li, Q. Zhang, H. Xu and K. S. Chan, Effects of van der Waals interaction and electric field on the electronic structure of bilayer MoS_2, *J. Phys.: Condens. Matter*, 2014, **26**(40), 405302.

67 D. Sánchez-Portal, E. Artacho and J. M. Soler, Analysis of atomic orbital basis sets from the projection of plane-wave results, *J. Phys.: Condens. Matter*, 1996, **8**(21), 3859.

68 R. S. Mulliken, Electronic population analysis on LCAO–MO molecular wave functions. I, *J. Chem. Phys.*, 1955, **23**(10), 1833–1840.

69 F. L. Hirshfeld, Bonded-atom fragments for describing molecular charge densities, *Theor. Chim. Acta*, 1977, **44**, 129–138.

70 M. Mousavi-Khoshdel, E. Targholi and M. J. Momeni, First-principles calculation of quantum capacitance of codoped graphenes as supercapacitor electrodes, *J. Phys. Chem. C*, 2015, **119**(47), 26290–26295.

71 B. A. Ali, A. M. Omar, A. S. Khalil and N. K. Allam, Untapped potential of polymorph MoS_2: tuned cationic intercalation for high-performance symmetric supercapacitors, *ACS Appl. Mater. Interfaces*, 2019, **11**(37), 33955–33965.